Eidgenössische Technische Hochschule Zürich
Swiss Federal Institute of Technology Zurich

Irma Telarovic

Probing Spatiotemporal Fractionation on the Preclinical Level

Master Thesis

Institute for Biomedical Engineering
Swiss Federal Institute of Technology (ETH) Zürich

Supervision

Prof. Dr. Martin Pruschy
Prof. Dr. Jan Unkelbach
Co-Supervisor: Prof. Dr. Antony Lomax
Tutor: Ivo Grgic

September 2018

Acknowledgements

Hereby, I would like to express my gratitude to everyone who helped me during this thesis project. First and foremost, I would like to thank my supervisors, Professors Martin Pruschy and Jan Unkelbach, for giving me the opportunity to do my master thesis in their research groups and for always being enthusiastic, motivating, present, patient and ready to help. I would also like to thank my co-supervisor, Professor Anthony Lomax, for his support over the choice of my project.

Special thanks to Dr. Jerome Krayenbühl for his help with the development and implementation of the project.

Furthermore, I would like to thank all the members of the Pruschy group, and especially Ivo Grgic, for always answering my questions, giving me advice and making me feel welcome. Your friendliness and support have made my stay a great learning experience that I will happily remember.

I also thank the Department of Visceral Surgery and the Department of Histology at the University Hospital Zürich, for excellent technical support and the Biologisches Zentrallabor of the University Hospital of Zürich for animal housing.

Finally, I'd like to thank my family for their understanding and support, especially during the writing process.

Contents

Abstract

Objective
In contrast to conventional radiotherapy, spatiotemporally fractionated (STF) treatments deliver a distinct dose distribution in each fraction. The aim is to increase the therapeutic window by simultaneously achieving partial hypofractionation in the tumor along with near uniform fractionation in normal tissues. This approach has previously been studied *in silico* based on the working hypothesis that different parts of the tumor can be treated in different fractions, as long as the cumulative biological dose that each part receives corresponds to the prescribed dose. In this thesis, an initial step is taken towards verifying this assumption in an experimental animal model.

Methods
To perform partial tumor irradiation in a small animal model, first a pipeline was developed combining a dedicated small animal image-guided research platform (X-RAD SmART/SmART-Plan, Precision X-Ray Inc.) with the clinical software MIM (MIM Software Inc.). The tumor growth delay of conventionally treated xenografts was then compared to a reductionistic preclinical model of STF. Upon reaching the tumor volume of 300 mm^3 $\pm$ 10%, animals were successively assigned to four treatment groups. The "No IR" group was sham irradiated. The "Half IR" group was irradiated with a dose of 12 Gy covering only one half of the tumor. The "STF IR" group received two partial irradiations separated by 24 hours, delivering 12 Gy each. The "Full IR" group received two partial irradiations delivering 12 Gy each as in the "STF IR" group, but applied successively. Tumor volumes were determined by daily caliper measurements and CT-based volumetry. Additionally, an immunohistological study was undertaken to investigate the DNA damage- and tumor microenvironment-related endpoints in the broader context of partial tumor irradiation.

Results
Tumors irradiated to the same dose, either immediately or with a 24 hour delay between two partial irradiations, exhibited no differences in the growth delay study. A reduction in the irradiated volume resulted in an intermediate response. CT-based volumetry measured overall significantly smaller starting volumes with an increased dispersion compared to the caliper-based volumetry, while the relative tumor growth curves (each point normalized to the corresponding initial volume) did not differ between the two methods. On the histological level, in tumors that received the first partial irradiation 24 hours prior to the second partial irradiation, there was a decrease in the incidence of double-strand DNA breaks in cells covered by the second irradiation. An increase in the microvessel density was found in partially irradiated tumors compared to other treatment groups.

Conclusion
The assumption of STF that the tumor response can be predicted by locally adding up biological doses from each fraction is supported in a reductionistic preclinical model whereby xenografts irradiated either immediately or with a 24 hour delay between two partial irradiations exhibited no difference in the growth delay study. Furthermore, the study suggests caliper- and CT-based volumetry to be interchangeable when considering relative, but not absolute volumes in tumor growth delay studies. Finally, the investigation of the effects of STF on the histological level suggests possible differences in the response of tumors to partial irradiation.

List of Abbreviations

AVM	Arteriovenous Malformation
AUC	Area Under Curve
BED	Biologically Effective Dose
CAIX	Carbonic Anhydrase Isozyme IX
CALVM	Caliper-Based Volumetry
CAR	Chimeric Antigen Receptor
CBCT	Cone-Beam Computed Tomography
CTV	Clinical Target Volume
CTVM	CT-Based Volumetry
DNA	Deoxyribonucleic Acid
DSB	Double-Strand Break
DVH	Dose-Volume Histogram
E_{photon}	Incident Photon Energy
eV	Electron Volt
GTV	Gross Tumor Volume
Gy	Gray
HI	Homogeneity Index
HR	Homologous Recombination
ICRU	International Commission on Radiation Units and Measurements
IGRT	Image-Guided Radiotherapy
IMRT	Intensity-Modulated Radiation Therapy
IR	Irradiation
ISL	Isodose Line
LET	Linear Energy Transfer
LQM	Linear-Quadratic Model
NHEJ	Non-Homologous End Joining
PECAM	Platelet Endothelial Cell Adhesion Molecule
RCF	Radiochromic Film
RT	Radiotherapy
SBRT	Stereotactic Body Radiation Therapy
SP	SmART-Plan
SSB	Single-Strand Break
STF	Spatiotemporal Fractionation
Z	Atomic Number

Chapter 1

Introduction

1.1 Malignant Disease

Malignant disease, an expression used interchangeably with cancer, is an umbrella term for a wide group of illnesses. This diverse group is characterized by uncontrolled growth and spread of abnormal cells, capable of invasion and destruction of both nearby and distant tissues [1].

In spite of continuous advances being made in both treatment and understanding the biology of the disease, cancer is still a major challenge for modern medicine. Globally, it is the second leading cause of death and is estimated to account for 9.6 million or 1 in 6 deaths in 2018. Most common cancer sites include lung, breast, colorectum and prostate. As a cause of death, lung cancer is dominant, followed by the cancer of colorectum and stomach (Figure 1.1) [2].

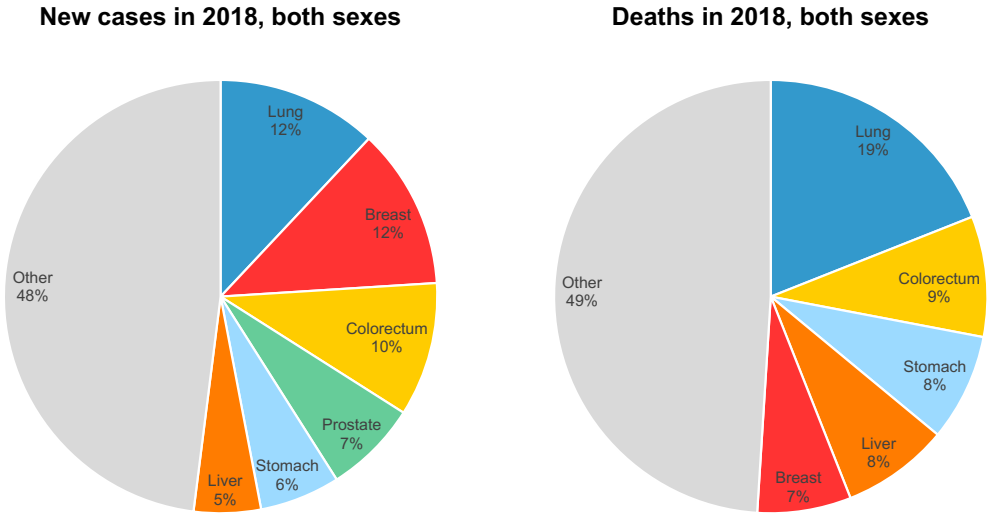

Figure 1.1: **Cancer statistics for 2018.** It is estimated that 18 million people will be diagnosed with cancer in 2018, most common being lung cancer and breast cancer (12% each). All together, malignant disease will account for 9.6 million deaths. The majority of these (19%) will be due to lung cancer. Adapted from [2].

1.1.1 Biology and Etiology of Cancer

For the majority of patients, the precise etiology of the disease is unknown. Only a handful of cancer syndromes, where a mutated gene in the germ line is clearly identified, are described. These include entities such as ataxia telangiectasia, neurofibromatosis and retinoblastoma. In the majority, the exact extent to which an individual genetic background contributes to the development of the malignancy remains largely unknown. Similarly, a variety of environmental factors are associated with the development of cancer, although precise mechanisms and the level of impact are still debated. Most commonly implicated environmental factors include tobacco and alcohol use, dietary factors, exposure to ultraviolet light, arsenic, certain infectious agents, medications and ionizing radiation [1].

Hallmarks of Cancer

Malignant transformation is thought to be the consequence of a multistep process resulting from a complex interplay between genetic predisposition and environmental factors. It is believed that this multistep process leads a healthy human cells through a series of premalignant states. During this process, cells progressively accumulate mutations which offer a growth advantage, essentially going through an "evolution" which culminates in the development of cancer [3, 4].

Hanahan and Weinberg developed this theory further in 2000 [3] by establishing six functional capabilities that are suggested to be necessary and sufficient for most, if not all malignancies. The original six hallmarks were extended by the authors in 2011 [4] to incorporate two emerging hallmarks and two enabling characteristics. These hallmarks include sustaining proliferative signalling, evading growth suppressors, activating invasion and metastasis, enabling replicative immortality, inducing angiogenesis, resisting cell death, avoiding immune destruction and deregulating cellular energetics. The two enabling characteristics are considered to be genome instability and tumor-promoting inflammation (Figure 1.2). These advances have lead not only to better understanding of cancer biology, but also to the development of novel treatment approaches that target specifically the different hallmarks.

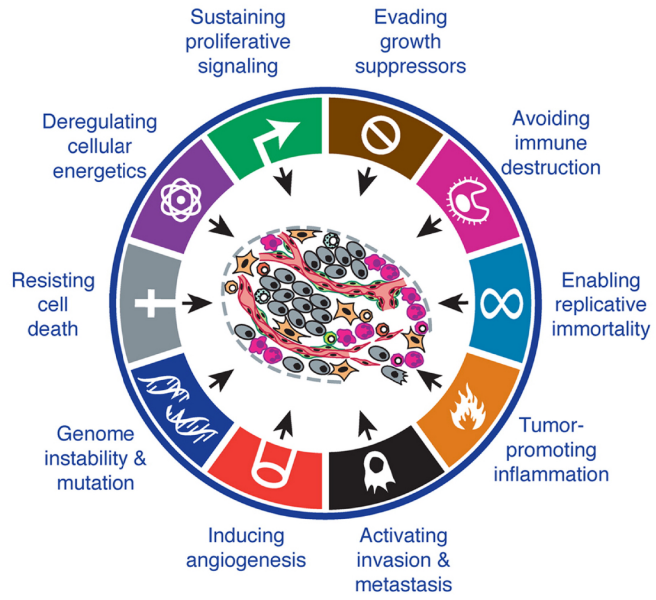

Figure 1.2: **Hallmarks of cancer.** Eight functional capabilities, together with two enabling characteristics, thought to be fundamental to the development of malignant transformation. Adapted from [4].

1.1.2 Cancer Treatment Strategies

Adapted from [1].

Depending on the type and stage of the tumor, as well as on the performance status of the patient, treatment strategies vary. Considering the endpoint, treatment can either be curative or palliative. Curative approach refers to a treatment aimed at completely removing the disease, while palliative approach aims at relief of tumor symptoms, preservation of quality of life and prolongation of life. Considering the area where the treatment measure is applied, the approach is either local or systemic. Local treatment approaches include surgery and radiotherapy (see next section), while systemic approaches refer to chemotherapy, endocrine therapy, biological therapy (includes immunotherapy) and targeted therapy. A benign neoplasm is most commonly treated by a surgical procedure only, while malignancy usually demands for a combined local and systemic approach.

Surgery

Surgery is a local solid tumor treatment modality rarely used as a sole approach and usually preceded or followed by radiotherapy and/or systemic therapy. Around 60% of patients will undergo a surgical procedure during their treatment [5]. It is performed as a part of staging, a curative or a palliative procedure.

Chemotherapy

Chemotherapy refers to systemically administered cytotoxic drugs that elicit a therapeutic response by interfering with cell division. By definition, chemotherapeutics are not cancer specific (i.e. are not targeted therapy) and interfere with different stages of the cell cycle of all cells. However, it is still possible to achieve a therapeutic effect while sparing the normal tissue by exploiting the differences between healthy and transformed cells. Cancerous tissue experiences an increase in the proliferation rate and has a decreased repair capacity [6]. For this reason, chemotherapeutic drugs are given over a period of days or weeks, which ideally allows the normal tissue to recover, while the tumor accumulates damage and is ultimately depleted (Figure 1.3).

The dose, and thereby the success, of the treatment is still limited by how much the normal tissue can tolerate, especially for the fast proliferating tissues, such as the bone marrow and the gastrointestinal tract. To avoid rapid development of resistance, usually a combination of drugs with non-overlapping mechanisms of action are given. Chemotherapy alone is the mainstay of the treatment of hematological malignancies. For solid tumors, it is usually used in combination with other treatment modalities.

Endocrine Therapy

Endocrine therapy interferes with the hormone system and can therefore successfully induce regression and maintain remission of a subgroup of cancers positive for hormone receptors. It is commonly used as an adjuvant treatment for breast and prostate cancer.

Biological Therapy

Biological therapy includes interferons, interleukins, immunotherapy and immunomodulatory drugs. These work by enhancing the function of the host immune system to overcome the evasion of the immune destruction, one of the hallmarks of cancer [4]. With the advancements in bioengineering, immunotherapy is becoming especially important, with chimeric antigen receptor (CAR) T-cells emerging as a promising therapy for a wide range of cancers [7].

Targeted Therapy

Targeted therapy encompasses monoclonal antibodies and intracellular signal inhibitors, whose development has been made possible by recent advances in molecular cancer research. Considering their specificity for molecular features associated primarily with cancer, these molecularly targeted agents offer advantages over conventional chemotherapy. However, identification of appropriate targets for a wide variety of cancers remains a challenge [8].

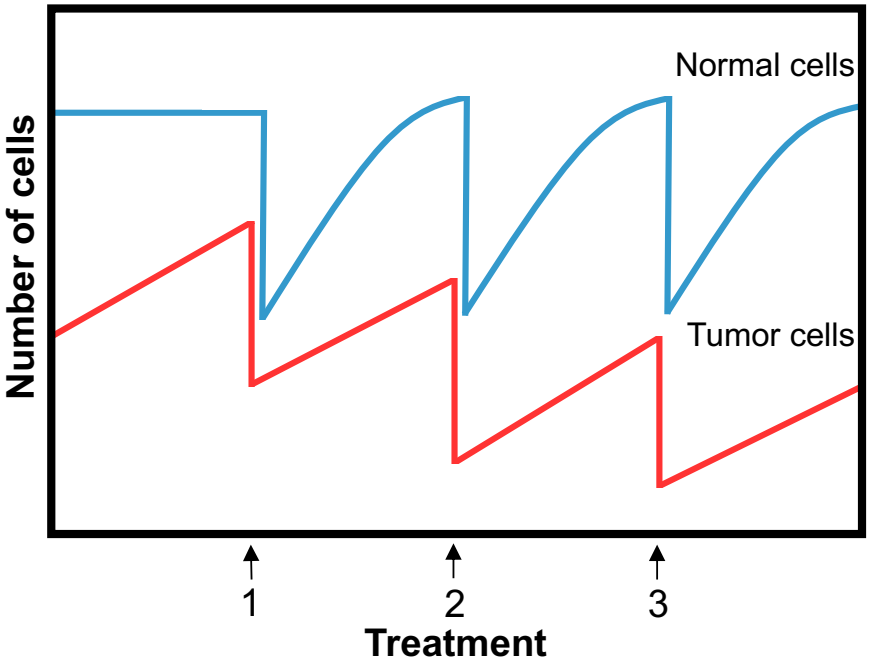

Figure 1.3: **Effects of the intermittent chemotherapy principle**. Chemotherapeutic drugs are typically given over the course of weeks or months to exploits the differences between normal and transformed tissue. Cancer exhibits higher proliferation rates and lower repair capacities compared to the healthy tissue, which results in gradual depletion of the cancer, while normal tissue ideally recovers between subsequent chemotherapy sessions. Adapted from [1].

Note: Approaches to treating hematological (leukemia, lymphoma) and solid cancers cancers are significantly different. Since the focus of this work is on solid tumors, treatment strategies described above pertain primarily to solid, rather than hematological cancers.

1.2 Fundamentals of Radiotherapy

Radiotherapy (RT) refers to the use of ionizing radiation in cancer treatment. It has been used in medicine since shortly after the discovery of X-rays in 1895. Together with surgery, RT is the mainstay of local treatment of cancer. Currently, approximately 50% of cancer patients undergo RT, either alone or in combination with other treatment modalities [9].

A distinctive feature of the science behind RT, as opposed to other treatment strategies, is its inherent interdisciplinarity. To successfully harm to tumor, while protecting the normal tissue, treatment planning needs to rely on detailed knowledge of both medical physics and radiobiology.

1.2.1 Physics of Ionizing Radiation

Ionizing radiation is the type of radiation able to excite and ionize atoms (i.e. release electrons) of the matter with which they are interacting. There are different types of ionizing radiation, including

γ-rays and X-rays, fast electrons, neutrons and heavy charged particles, such as α particles, protons and carbon ions. γ-rays and X-rays both refer to photons and differ only in their origin: X-rays are generated by bremsstrahlung i.e. slowing down of charged particles with high velocities in an X-ray tube, while γ-rays refer to photons emitted by radioactive nucleus or in an annihilation process. Currently, high-energy X-rays are the most commonly used type of ionizing radiation in RT, primarily for external beam RT. Other modes of RT include brachytherapy and systemic application of radionuclides [10, 11]. In this work, a dedicated small animal X-ray-based external beam RT platform was used and therefore the following section will focus on photon beams.

Photon Beams

A photon is both a particle and an electromagnetic wave. It has no mass and no charge and it travels at the speed of light. It is usually characterized by the amount of energy it carries, expressed in electron volts (eV). For small animal RT as well as for imaging purposes in humans, usually photons in the keV range are used. For RT in humans, MeV photons are applied [10, 11, 12].

Being uncharged, a photon is considered an indirectly ionizing particle. This means that, as opposed to directly ionizing particles, a photon will not cause ionizations on its own but must first transfer its energy to a charged particle which can then carry on to ionize the material. The damage caused by photons is therefore considered indirect and is mediated by secondary particles, in this case electrons [6].

Photon Interactions with Matter

The transfer of energy from photons to electrons occurs through five types of interactions, depending on the energy of the photon and the properties of the irradiated material (Figure 1.4). These are: (1) Compton effect, (2) photoelectric effect, (3) pair production, (4) Rayleigh scattering and (5) photonuclear interactions. In the energy ranges used in RT, energy transfer occurs primarily through the first three interactions (Figure 1.5) [10, 11].

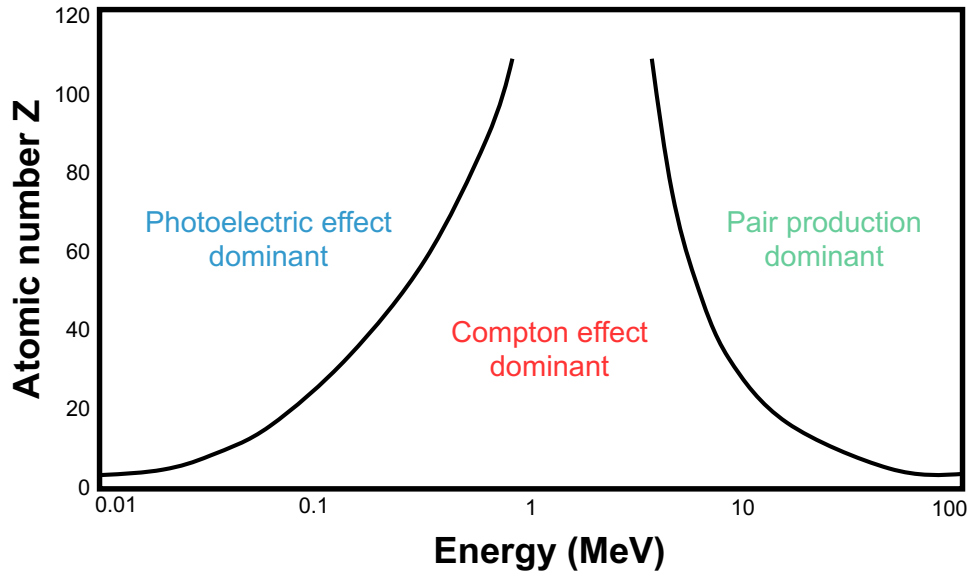

Figure 1.4: **Relative importance of photon interactions depending on the photon energy and the atomic number of the absorber (Z).** Compton effect dominates in a broad range of energies relevant for medical physics. Photoelectric effect becomes increasingly important for low energies and high Z numbers. Adapted from [13].

- **Photoelectric effect** occurs when a photon collides with a tightly bound electron and transfers all of its energy (E_{photon}). Some of this energy is used to overcome the binding energy of the electron and eject it from the atom, while the rest is transformed into kinetic energy of the electron. The result of this interaction is a free electron. The probability of the photoelectric effect is approximately proportional to the third power of the atomic number (Z^3) and to $(1/E_{photon})^3$. Therefore, it is important for high Z materials and lower energies, such as those used in small animal radiation therapy and in medical imaging. As a consequence of the high Z-dependence, the dose absorbed by tissues with high effective atomic numbers (such as the bone) is increased [10].
- **Compton effect** takes place when the impinging photon only gives up a part of its energy and transfers it to a loosely bound electron. The photon is now scattered and has lost some of its energy, while the electron is ejected and can go on to ionize the material. In contrast to the photoelectric effect, Compton effect is virtually independent on the atomic number. It is the dominant type of interaction approximately in the range from 50 keV to 3 MeV. This makes it the most important interaction when considering the range of energies used in human therapy. In small animal RT and in medical imaging, energy absorption takes place both through the Compton effect and the photoelectric effect [10].
- **Pair production** results in disappearance of the incident photon and leads to the creation of two particles, an electron and a positron. Since the mass of an individual electron/positron is 511 keV, the minimal energy required for pair production is 2 * 511 keV = 1.02 MeV [10].

	Photoelectric effect	Compton effect	Pair production
10 keV	> 99%	-	-
200 keV	< 1%	> 99%	-
2 MeV	< 0.1 %	~ 99%	~ 1%
20 MeV	-	~ 50%	~ 49%

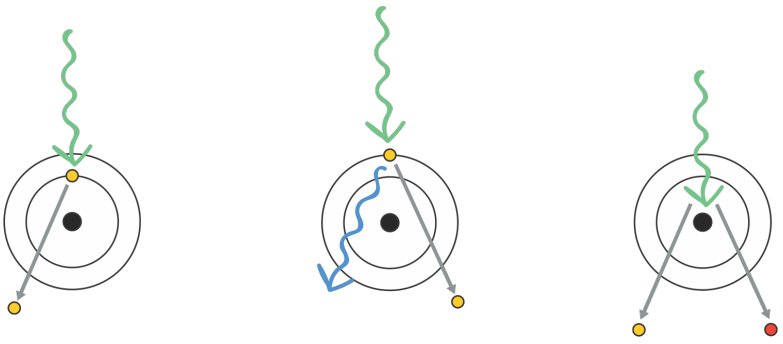

Figure 1.5: **Overview of photon interactions with matter in energy ranges relevant for RT.** Compton effect dominates in the energy ranges used in RT and at the higher end of energies used in medical imaging. Photoelectric effect takes over in the lower end of energies used in medical imaging. For pair production to occur, a minimum of two times the rest mass of an electron is needed i.e. 1.02 MeV. yellow = electron, green = incident photon, blue = scattered photon, red = positron. Adapted from [14].

The Experience of a Single Incident Photon

During RT, when a single photon comes in contact with the patient, the probability of an interaction to take place is low. Most probably, the photon will pass through without consequences for the tissue. In the unlikely case that either photoelectric of Compton effect take place, an electron is produced. Unlike photons, electrons are charged particles with a very high probability of interacting with matter. A single electron can set a chain reaction in motion by ionizing and exciting the surrounding material, leading to a "splash of electrons". For example, production of a single electron by a 4 MeV photon undergoing Compton scattering will lead to up to 40 000 ionizations until all energy is lost. Therefore, only one interaction of the incident photon will result in ionizations in tens of thousands of atoms. It is important to note that these ionizations and therefore the resulting damage to the tissue are always mediated by secondary electrons and are not produced directly by the photon [11].

1.2.2 Molecular Radiobiology

Upon interaction and subsequent secondary electron production, a series of ionizations and excitations are produced in the tissue, leading to lesions in either a direct or indirect way. Direct action refers to direct absorption of the radiation by a critical target (i.e. biological macromolecule, including DNA, RNA, proteins), and is largely attributed to densely ionizing particles, such as α-particles, carbon ions and neutrons. Sparsely ionizing particles, including photons, cause only about a third of the damage by direct action. The majority of damage caused by photons is the result of an indirect action. Indirect action refers to absorption of the radiation by the medium (particularly water) and subsequent production of free radicals. Free radicals are highly chemically unstable molecules able to move within a range of 2 nm and disrupt the structure of the surrounding biological macromolecules [6, 15].

DNA Lesions

Deoxyribonucleic acid (DNA) is believed to be the principal target for both the cytotoxic and mutagenic effects of radiation [6]. The damage can manifest in various forms, including alterations to and loss of bases and sugars, intra- and interstrand crosslinking, single-strand breaks (SSB) and finally double-strand breaks (DSB). 1 Gray (Gy) i.e. absorption of 1 joule of radiation energy per kilogram of matter results in approximately 1000 base damages, 1000 SSB and 20-40 DSB per cell. Although initially less abundant, DSB are considered the most lethal form of radiation-induced damage due to the difficulty of repairing such a lesion [16]. Notably, just one DSB in a vital section of DNA that remains unrepaired may be sufficient to kill the cell [15].

DNA Repair

Mammalian cells have a variety of specialized pathways available to sense and repair different forms of damage to DNA. Most DNA lesions are readily repaired by using the opposite strand as a template in the processes of base excision, nucleotide excision, crosslink repair, mismatch repair and SSB repair. In the case of DSB, however, a template is not always readily available. During G1 phase of the cell cycle, only a single copy of DNA is present in the cell, leading to an error-prone repair process (non-homologous end joining, NHEJ). On the other hand, DSB occurring during S and G2 phases result primarily in an error-free repair (homologous recombination, HR) due to the presence of a sister chromatid that serves as a template [6, 16].

Radiation-Induced Biomarkers

Various biomarkers may be analyzed in radiobiological studies to investigate the impact of radiation on different levels. As a part of this thesis, a histological examination was performed to compare how different RT schedules affect the tumor tissue on the microscopic level. The endpoints were as follows:

- **DNA damage and repair (γ-H2AX)**
  Since DSB are the most lethal form of radiation induced damage, visualization and quantification of these sites is of interest for investigation of both DNA damage induction and repair. In response to DSB formation, a variant of the histone H2A (H2AX) is rapidly phosphorylated to produce γ-H2AX. This form of the histone then acts as a recruiting agent for the DNA repair machinery [17, 18]. By using immunofluorescence-based assays, it is possible to reliably detect γ-H2AX and subsequently analyze the initial DNA damage (at 30 minutes post irradiation) and the efficiency of DNA repair (at 24 hours post irradiation) [19, 20].

- **Microvessel density (CD31)**
  The vascular network in a neoplastic tissue is fundamentally different from normal vasculature. Blood vessels of the tumor microenvironment are typically disorganized and aberrant, which results in a chaotic and largely dysfunctional vascular network [21]. This is a consequent to a complex interplay of the hallmarks of cancer [4], ultimately leading to sustained proangiogenic and provasculogenic signalling and subsequent aberrant neovascularization [21]. The extent of neovascularization has been implicated as a prognostic factor in cancer, with an increased tumor microvessel density correlating with aggressiveness [22]. Moreover, changes in the microvessel density in response to RT have been associated with radiosensitivity of the tumor and the overall treatment response [23, 24]. CD31 or platelet endothelial cell adhesion molecule (PECAM-1) is an endothelial cell surface antigen commonly used to visualize endothelial cells and thereby quantify the microvascular density in the tumor [25].

1.2.3 Dose Fractionation

X-rays were first used to treat cancer only a few years after their discovery in 1895. It soon became apparent that the biological effects of the physically equal doses differ depending on how this dose is delivered over time. Based on clinical observations in the following years, it was widely established that the dose delivered in multiple fractions results in the improvement of the therapeutic index (i.e. the ratio between the efficacy and toxicity) [26, 27].

The Rs of Radiotherapy

The empirical evidence gathered from early clinical observations was followed with a number of radiobiological studies throughout the 20th century. The knowledge acquired by these studies formed the basis of the modern fractionated RT and was conceptualized by Withers in 1975 as the "4 Rs of Radiotherapy" [28]. These four mechanisms remain the paradigm of differential response of the neoplastic and normal tissue to dose fractionation. They are as follows [6, 15, 28]:

- **Repair**
  Depending on the dose and the capacity of the cell, the damage done by ionizing radiation may be reversed in the process of sublethal damage repair. This phenomenon is apparent from an increase in cell survival in response to delivery of an equal physical dose in two fractions versus one. It is attributed to the ability of the cell to partially or completely repair the damage done by the first fraction prior to the delivery of the second fraction. If the time interval between to two fractions is not sufficient, the damage may accumulate and result in a lethal event. This depends on the capacity of an individual cell to repair the sublethal damage, and is postulated to be significantly lower in malignant compared to normal cells. Therefore, repair primarily allows for normal tissue to recover in between fractions. However, it also renders the tumor more resistant to RT, albeit to a limited degree due to the inferior repair capacity of malignant cells.

- **Redistribution**
  The sensitivity of the cell to ionizing radiation is known to depend on the cell cycle. Generally, cells in the S phase are considered most resistant, while the cells in late G2/M phase tend to be the most sensitive. In an unirradiated tissue, cells are asynchronous and therefore the

radiosensitivity varies considerably. In a single fraction, sensitive cells will likely be killed, leaving the surviving population synchronized in the resistant cell cycle phase. These cells will then progress through the cell cycle and ideally reach the sensitive phase by the time the second fraction is applied. Consequently, redistribution causes an increase in the sensitivity of both the tumor and rapidly dividing normal tissues but does not affect slowly dividing normal tissues.

- **Repopulation**
  Apart from repair, cell survival may increase due to cell division. The process of repopulation, however, is much slower than repair and this effect is important on the level of the overall treatment duration rather than the time in between fraction. Rapidly dividing normal tissues benefit from repopulation during fractionated treatment, although this also increases the resistance of the tumor to RT. Moreover, it has been shown that RT can trigger "accelerated repopulation" in the neoplasm, leading to an increase in the division rate and rendering the tumor more resistant.

- **Reoxygenation**
  The response of cells to ionizing radiation strongly depends on oxygen. Prior to irradiation, a tumor typically contains a mixture of normoxic and hypoxic cells. Hypoxic cells are more resistant and a single fraction is likely to kill normoxic cells, while the hypoxic fraction survives. Therefore, immediately after irradiation, tumor is largely composed of hypoxic cells. However, if sufficient time passes prior to the next fraction, the process of reoxygenation occurs in which a proportion of the cells becomes normoxic and therefore sensitive to radiation. As a consequence, reoxygenation makes the tumor more sensitive to RT.

In 1989, an additional "R" was proposed by Steel et al. [29]:

- **Intrinsic radiosensitivity**
  Intrinsic radiosensitivity refers to the inherent variability observed in the response of different cells to RT. Depending on the genetic alterations in the intracellular pathways relevant to RT, tumors of the same histological type might respond differently to the treatment. Identification of these molecular changes can help predict the response and thereby modify the treatment as necessary.

The Linear-Quadratic Model

In radiobiology, the dose-response relationship is typically shown on a semi-logarithmic plot that describes the relationship between the radiation dose and the proportion of the cells that survive. For low linear energy transfer (LET) types of ionizing radiation i.e. sparsely ionizing radiations, such as X-rays, the resulting survival curve is initially straight, then bends over a range of a few Gy and finally straightens up again at very high doses. For densely ionizing radiations i.e. high LET, the curve is a straight line [6].

A cell survival curve for photon RT is most widely mathematically described with the liner-quadratic model (LQM) (Figure 1.6). This is a second order polynomial that fits a continuously bending curve. Cell survival is predicted by:

$$-ln(S) = \alpha D + \beta D^2 \tag{1.1}$$

$$S = exp(-\alpha D - \beta D^2) \tag{1.2}$$

where S is the cell survival fraction and D is the dose. It is assumed that αD, the linear component of the model, results from the single-track events (i.e. a lethal event caused by a single photon), while the quadratic component, (βD^2), corresponds to two-track events.

The linear and quadratic components are equal when

$$\alpha D = \beta D^2 \tag{1.3}$$

$$D = \alpha/\beta \tag{1.4}$$

This α/β ratio is used to describe the shape of the curve. High α/β values correspond to steeper ("more exponential") curves with the α term dominating, while the β term becomes larger as the curve becomes "bendier". Overall, the LQM describes the survival curves well in the ranges of low to mid doses. For high doses, the LQM curve continues to bend, while in reality the dose-response relationship starts resembling a straight line [6, 15].

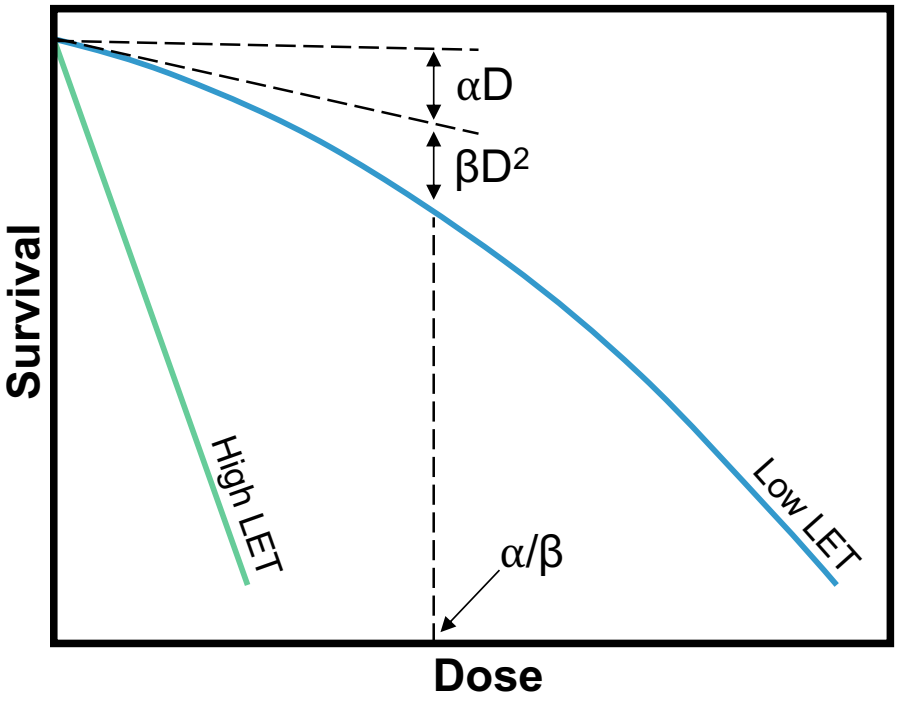

Figure 1.6: **Linear-quadratic model of cell killing.** LQM uses a second order polynomial to predict the surviving fraction. High LET radiation results in a straight line with the linear α term dominating, while the low LET curve depends both on the linear (α) and quadratic (β) terms. The dose at which the linear curve corresponds to the quadratic curve is termed the α/β ratio and is used to describe the curve. Adapted from [15].

Early-Responding and Late-Responding Tissues

In the context of fractionated RT, tissues can be considered in two distinct groups: early-responding and late-responding. The differences between the two types are clearly reflected in the "bendiness" of the corresponding cell survival curves (Figure 1.7). As mentioned in the previous section, this can be described by the α/β ratio [6, 15].

Early-responding tissues include the tumor tissue and normal tissues with a high cell turnover, such as the skin, intestinal epithelium and the hematopoietic system. The dose-response curves for such tissues are more straight, with relatively small "shoulders" and the linear term dominating. The α/β ratio of early-responding tissues is considered high, and is typically around 10 Gy [6, 27].

Late-responding tissues, on the other hand, exhibit a more curved dose-response relationship, with a larger "shoulder|. The α/β ratio is smaller, around 2 to 3 Gy. Typical late-responding tissues include the spinal cord, kidney, lung, heart, bladder and the central nervous system [6, 27].

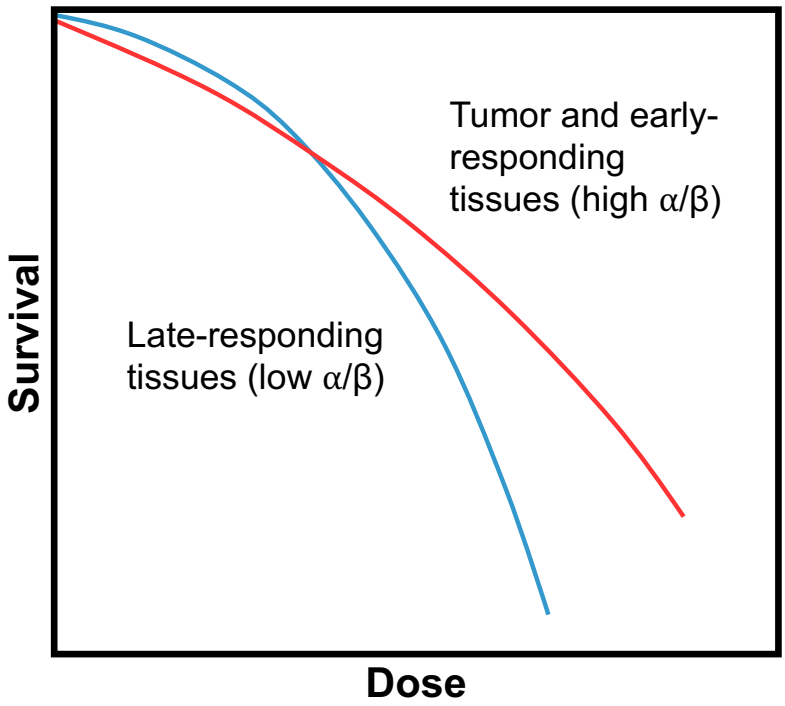

Figure 1.7: **Representative cell survival curves for early- and late-responding tissues.** Early-responding tissues, including neoplastic tissues, exhibit a larger α/β ratio i.e. a less curvy dose-response relationship. Late-responding tissues show a smaller α/β ratio and a curvier dose-response relationship. Adapted from [30].

Fractionation Schedules

Depending on the dose per fraction, time between fractions and the overall treatment time, we can consider several different fractionation schedules. Based on the "Rs of Radiotherapy" and the concept of early- and late-responding tissues, the determinants of different fractionation schedules can be summarized as follows (Table 1.1) [6, 31]:

- **Fraction size** determines the extent of lethal and sublethal damage. Cells can counteract sublethal damage by initiating the DNA repair response. Lethal damage is by definition irreversible. Fraction size is the dominant effect in determining "late reactions" i.e. the damage done to late-responding tissues, since these tissues do no undergo repopulation or redistribution during an average RT treatment. Late reactions are defined as side effects occurring more than 90 days after the start of RT.

- **Time between fractions** allows the cells to initiate and execute repair of the sublethal damage, determined by the fraction size. If the time allowed between subsequent fractions is not sufficient, the cell accumulates sublethal damage which eventually leads to a lethal outcome. In this context, time between fractions is a factor in response for all tissues, including the tumor and both early- and late-responding tissues. For early-responding tissues and the tumor, it is also important to consider reoxygenation and redistribution, which may take place during this time and increase the sensitivity to radiation.

- **Overall treatment time** is determined by the total dose, the size of the fractions and time between fractions. For late-responding tissues, overall treatment time has little influence. Due to the effect of repopulation and the occurrence of accelerated repopulation, the overall treatment time is significant for the tumor control and early-responding tissues.

Table 1.1: **Effects of changing the determinants of fractionation schedule on sensitivity of different tissues to radiation.** Effects in red increase the tumor resistance and the occurrence of side effects. Effects in blue render the tumor more sensitive and the normal tissue more resistant to radiation.

	Tumor	**Early-responding tissue**	**Late-responding tissue**
↑ Fraction size	↓ repair	↓ repair	↓ repair
↑ Interfraction time	↑ repair ↑ reoxygenation ↑ redistribution	↑ repair ↑ redistribution	↑ repair
↑ Total time	↑ repopulation ↑ reoxygenation	↑ repopulation	no influence

Taking all this into account, it is evident that RT treatment is always a compromise between tumor control and normal tissue toxicity. Depending on the fraction size, time between fractions and the overall treatment time, several different schedules of fractionation can be considered [6]:

- **Conventional fractionation**
  Schedule: 1 fraction/day, 2 Gy/fraction, 5 days/week, 7 weeks
- **Hyperfractionation** [32]
  Rationale: twice as many fractions in the same overall time decrease late reactions while maintaining the repopulation effects
  Disadvantages: total dose needs to be increased to counteract the decrease of dose per fraction
  Schedule: 2 fractions/day, 1.2 Gy/fraction, 5 days/week, 7 weeks
- **Accelerated hyperfractionation treatment** [33]
  Rationale: multiple smaller fractions per day decrease both late reactions and the overall treatment time (i.e. repopulation effects)
  Disadvantages: severe early reactions and possible late reactions (myelopathy) due to time between fractions being too short
  Schedule: 3 fractions/day, 1.5 Gy/fraction, 12 consecutive days
- **Hypofractionation** [34]
  Rationale: certain tumors, such as prostate cancers, may have characteristics of late-responding tissues, which decreases the advantage of multiple fractions; acceleration counteracts repopulation and improves tumor control; advances in medical physics allow for more conformality in dose delivery, thus physically sparing the normal tissue
  Disadvantages: toxicity to normal tissues
  Schedule: 1 fraction/day, 2.67 Gy/fraction, 5 days/week, 3 weeks

Biologically Effective Dose

A brief overview of different fractionation schemes in the previous section already gives an idea of the complexity of dose fractionation in RT. Due to an interplay of a number of factors influencing the outcome of RT, there have been many attempts to come up with a simple way to compare different fractionation regimens [35, 36]. Today, the most widely used is the concept of the biologically effective dose (BED) based on the LQM, suggested by Barendsen [37] and Fowler [38]. According to the BED model, different fractionation schemes can be compared quantitatively by the BED number which is defined as follows:

$$BED = (nd)(1 + \frac{d}{\alpha/\beta}) \tag{1.5}$$

where n represents the number of fractions and d is the dose per fraction. The α/β ratio is the previously mentioned dose at which the linear component corresponds to the quadratic component,

and is a characteristic of the tissue.

The simplest form of the BED model stated above (Equation 1.5) has been proven useful by numerous studies and clinical reports and is widely applicable to conventional fractionation [6, 15, 39]. However, it considers only the size of the fraction, and not the dose rate, the time between fractions or the overall treatment time. Therefore, extensions are often necessary when considering modifications of conventional fractionation schedules and other specific situations. These extensions include, for example, the Lea-Catcheside time factor [40] that accounts for the different dose rate effects, the repopulation correction factor [41] that considers the proliferation of the tumor during the treatment and the resensitization term [42] that includes the effects of redistribution and reoxygenation into the model. Various other extensions and modifications, applicable to specific forms of RT such as radiosurgery, stereotactic body radiation therapy (SBRT), brachytherapy and high LET RT, are also available in the literature [43, 44, 45].

Overall, the BED concept is an easy-to-use, widely accepted method for isoeffective dose fractionation calculations based on the LQM. Although proven to be useful in many situations, due to its inherent limitations, it should always be used with careful consideration and appropriately extended or modified according to the setting.

1.3 Spatiotemporal Fractionation

As mentioned in the previous section, determining the fraction size, time between fractions and the overall treatment time is subject to a compromise between tumor control and normal tissue toxicity. Increasing the fraction size and decreasing the time between fractions and the overall treatment time generally improves tumor control on account of an increase in the normal tissue toxicity (Table 1.1). Ideally, neoplastic tissue would receive a higher dose per fraction (i.e. hypofractionation) while the dose to the healthy tissue remains given in a conventionally fractionated regimen. Spatiotemporal fractionation (STF), the primary focus of this thesis, is a novel approach to achieve these goals [46, 47, 48, 49, 50, 51].

1.3.1 Principles of Spatiotemporal Fractionation

As opposed to the traditional approach in which all fractions deliver the dose according to the same treatment plan, in STF the RT treatment plan is altered during the treatment course. The aim is to design the different fractions such that the normal tissue receives similar dose distributions in each fraction (corresponding to conventional fractionation) while each fraction delivers a high single dose to different regions of the tumor (corresponding to hypofractionation).

Cumulative BED

As explained above, the BED model is widely used to compare the effectiveness of different fractionation schemes [39]. For STF, a generalized form of the BED model is proposed [48, 50], whereby cumulative BED b_i in voxel i is given by :

$$b_i = \sum_{t=1}^{n} (d_{ti} + \frac{d_{ti}^2}{(\alpha/\beta)_i}) \tag{1.6}$$

where n is the number of fractions, d_{ti} is the physical dose delivered to voxel i in fraction t and $(\alpha/\beta)_i$ is the α/β ratio of the tissue that voxel i belongs to. With this model, it is assumed that different parts of the tumor can be treated in different fractions as long as each part of the tumor receives the prescribed cumulative biological dose in the end. For a quantitative interpretation, Equation 1.7 can be scaled by a factor:

$$\frac{1}{1 + \frac{X}{\alpha/\beta}} \tag{1.7}$$

where X is a reference dose level. Thereby, we can consider the equieffective dose EQDX [34]:

$$EQDX_i = \frac{b_i}{1 + \frac{X}{(\alpha/\beta)_i}} \tag{1.8}$$

We can interpret the EQDX as the total physical dose that needs to be delivered in a uniform treatment with X dose per fraction to achieve the same BED.

1.3.2 Applications and Limitations

Existing studies demonstrated the benefit of STF *in silico* in the context of cerebral arteriovenous malformations (AVMs) and liver tumors [48, 50, 51]. It was shown that, for a fixed prescribed target BED, it is possible to reduce the mean BED by 10% in the healthy brain tissue [48], and by 15-20% in the healthy liver tissue [50, 51]. The studies propose STF to be a beneficial approach in the following situations [48, 50]:

- **The target volume closely corresponds to the gross tumor volume (GTV).** In this case, tumor hypofractionation is feasible, as opposed to the situation when the target volume resembles the clinical tumor volume (CTV) with the embedded normal tissue that requires conventional fractionation.
- **The surrounding tissue is parallel i.e. mean dose is the limiting factor.** STF primarily lowers the mean dose to the healthy surrounding tissue. "Parallel" organs, such as the liver and the lung, benefit from this. They posses a functional reserve capacity and can sustain high local dose deposits as long as a critical volume of the tissue is still preserved. On the other hand, for "serial" organs, such as the spinal cord, there is a threshold dose above which there is loss of function, even if only given to a small volume [6].
- **The patient can be securely immobilized.** Setup uncertainty is an especially important potential issue with STF as it involves steep dose gradients and a dynamic fractionation scheme in which averaging over time is not expected.

1.4 Small Animal Radiation Research Platforms

In the RT, the size discrepancy between humans and small animals demands not only geometrical downscaling, but also a shift from MeV beams (typically used in human RT) to keV beams. Consequently, it is not possible to directly translate from a clinical system into an experimental animal model and a dedicated platform must be used. Due to technical demands of such small animal radiation research platforms, these have only recently been introduced. One of these state-of-the-art small animal image-guided radiation research platforms (X-RAD SmART) was used in this thesis together with a dedicated treatment planning system (SmART-Plan).

1.4.1 Requirements for Small Animal Irradiation

The necessity for dedicated small animal radiation research platforms stems from specific requirements associated with these systems that differ significantly from clinical systems. These are as follows:

- **Beam energy**
  MeV beams, used routinely in human RT, offer sufficient technical precision for humans. For small animals, however, this is not fulfilled, given that the sizes of buildup and re-buildup regions are on the order of the size of the animal itself. In addition, lateral beam penumbra for MeV beams may extend several millimeters beyond the geometric field [10, 52]. Therefore, to calculate and subsequently deliver a uniform and conformal dose to a tumor with reasonable accuracy, energy downscaling to the keV range is necessary [12].

- **Image resolution**
  A typical voxel size in humans ranges from 1 to 5 mm, while for mice, voxel sizes of 65 to 330 µm are required [53]. This is easily achieved by modern micro-CT scanners, however oftentimes spatial resolution must be sacrificed to allow for faster scanning and lower radiation dose [54].
- **Imaging dose**
  Imaging dose is a specific concern in small animal radiation therapy, especially for longitudinal studies where imaging procedure is repeated multiple times. In order to achieve a comparable signal-to-noise ratio as in conventional CT, but with significantly smaller voxel sizes, photon fluence must be increased accordingly. Thereby, depending on the system and imaging parameters, a full body micro-CT is reported to deliver between 10 and 70 cGy to an animal [55], which is approximately ten times compared to what a human receives during a similar procedure [56].
- **Targeting accuracy**
  While human tumors are on the order of several centimeters, mouse tumors are on the millimeter scale. Therefore, precision on the order of 0.1 mm rather than a few millimeters as in human therapy, is needed [53].
- **Treatment Planning**
  In the MeV energy ranges, Compton effect dominates and thereby reasonable accuracy in dose calculation can be achieved by considering only the difference in physical density between tissues obtained from the CT, while neglecting differences in the material composition. In the keV energy ranges, where photoelectric effects also becomes significant, both physical density and tissue composition play important roles in dose absorption. By neglecting the material composition in this case, significant dose calculation errors will arise as the photoelectric effects cross section increases with the increasing atomic number to the power of 3. Apart from this, clinical treatment planning systems are usually not designed to compute with a large number of small voxels typical for small animal studies and are usually intended for calculating with field sizes above 3 cm, which surpasses a typical field size in small animals. Therefore, treatment planning softwares used for humans are inadequate for direct translation to animal studies and designated treatment planning systems must be used [57].

1.4.2 X-RAD SmART

The X-RAD SmART, a small animal image-guided radiation research platform used in this thesis, was developed at the Princess Margaret Cancer Centre in Canada [12] and commercialized through Precision X-Ray Inc. It offers integrated precision irradiation with cone-beam computed tomography (CBCT) guidance and bioluminescence tomography in a single, self-shielded unit (Table 1.2). To allow for image-guided radiotherapy (IGRT), a rotating gantry and a three-axis computer-controlled animal couch are used along with an automated stage correction during irradiation. Both fixed field and dynamic arc (0°to 360°) dose delivery modes are available along with a set of interchangeable collimators of different sizes (from circular 1 mm to rectangular 40 mm x 40 mm).

Table 1.2: **X-RAD SmART specifications.** Due to a size discrepancy between humans and small animals, the requirements for a small animal radiation research platform differ from a clinical platform.

Beam energy	10-225 kVp
Dose rate	3 Gy/min
Image resolution	100 µm
Minimal beam diameter	1 mm
Targeting accuracy	up to 0.1 mm

1.4.3 SmART-Plan Treatment Planning System

SmART-Plan is a dedicated small animal treatment planning system developed in MATLAB by MAASTRO clinic in collaboration with Precision X-Ray [58]. Typical workflow (Figure 1.8) resembles closely to what is used in the clinics today. To start with, CT images of the animal (compliant with the DICOM standard) are imported into the software. Next, each pixel is assigned density and material. The conversion from Hounsfield units (HU) to physical density is done automatically according to previously obtained density calibration curve. Material assignment is then done manually by setting up ranges of HU that correspond to certain materials (up to 9 different materials can be assigned). The following step includes contouring, similar to what is done in the clinics. Both tumor and different normal tissues can be delineated for subsequent analysis of dose distribution. The treatment plan is then finalized by positioning the isocenter and setting the dose, field size and irradiation scheme (number of beams and corresponding angles). With this, the process is ready for a Monte Carlo dose calculation. Upon completion of the calculation, dose distribution is shown and a dose-volume histogram (DVH) is generated. The treatment plan can now be exported into X-RAD SmART and immediately executed.

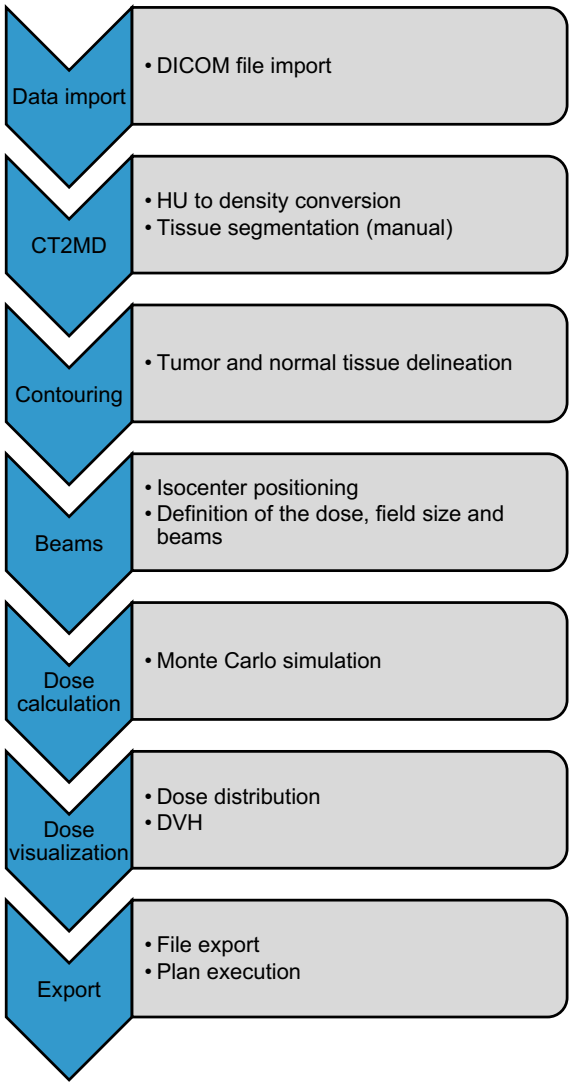

Figure 1.8: **SmART-Plan workflow.** The steps on the left side correspond to sections in the user interface. The content of each step is briefly described on the right.

Chapter 2

Aims of the Project

In contrast to conventional radiotherapy, spatiotemporally fractionated treatments deliver a distinct dose distribution in each fraction. The aim is to increase the therapeutic window by simultaneously applying a high dose hypofractionated radiotherapy to the target volume and a near uniform low dose fractionated radiotherapy in the surrounding normal tissue. This approach has previously been studied *in silico* by Prof. Unkelbach et al. in treatment planning studies based on the working hypothesis that different parts of the tumor can be treated in different fractions as long as the cumulative biological dose that each part receives corresponds to the prescribed dose.

The goal of this thesis is to do an initial step towards verifying the assumption of spatiotemporal fractionation that the tumor response can be predicted by locally adding up biological doses from each fraction in an experimental animal model.

Specifically, the thesis will focus on the following subprojects:

- **Overview of spatiotemporal fractionation**
  A brief overview will be given on the physical and radiobiological fundamentals behind fractionated radiotherapy and spatiotemporal fractionation specifically (Chapter 1).
- **Development of the pipeline for partial tumor irradiation**
  Prior to irradiation of the experimental animal models, a protocol will be be established with clear guidelines on treatment planning, execution and evaluation. This will include finding appropriate solutions and methods to (1) characterize and verify the dose distribution, (2) optimize the treatment planning workflow, define goals and constraints, (3) perform image registration to account for interfractional movement, (4) optimize fractionated dose homogeneity, (5) perform CT-based volumetry and finally (6) validate the complete pipeline (Section 4.1).
- **Influence of spatiotemporal fractionation on the tumor growth delay**
  In a reductionistic approach to verify the assumption of spatiotemporal fractionation, the growth delay of subcutaneous tumors treated with two partial irradiations (each covering exactly one half of the tumor) separated by 24 hours will be compared to the growth delay of tumors treated fully in one day. Tumor volumes will be determined by caliper- and CT-based volumetry (Section 4.2).
- **Effects of spatiotemporal fractionation on the histological level**
  A histological examination will be performed to investigate the effects of partial tumor irradiation on the initial DNA damage response, the tumor microenvironment and immunological endpoints (Section 4.3).

Chapter 3

Materials and Methods

3.1 Materials

Crystal violet	Merck
Dimethylsulfoxid (DMSO)	Sigma-Aldrich
Dulbecco's Modified Eagle Medium (DMEM)	Gibco/GlutaMAX, Thermo Fischer Scientific
Ethanol (EtOH)	Merck
Fetal Bovine Serum (FBS)	Gibco, Thermo Fischer Scientific
Formalin	Kantonsapotheke Zürich
Glycerol	Sigma-Aldrich
Isoflurane	AbbVie
Methanol (MeOH)	Morphisto
Mycoplasma Detection Kit	Lonza
Paraffin	Merck
Phosphate Buffer Solution (PBS)	Kantonsapotheke Zürich
Penicillin/Streptomycin (P/S)	Gibco, Thermo Fischer Scientific
Trypsin	Gibco, Thermo Fischer Scientific

3.1.1 Radiochromic Films

The same batch of Gafchromic EBT3 film was used for all dosimetric studies. Gafchromic RTQA2 was used for qualitative analysis and relative dosimetry.

3.1.2 Ionization Chamber

A Farmer type ionization chamber (model TW30012, PTW) was used for reference dosimetry. The chamber has a sensitive volume of 0.6 cm^3 and was calibrated for energies ranging from 90 kV to 280 kV by the Institut de Radiophysique in Lausanne. The calibration certificate provides correction factors to convert a charge measured with the calibrated chamber to dose to water under reference conditions.

3.1.3 Animals

Eight week old female C57BL/6J mice were ordered from Envigo. All animals were maintained under specific pathogen-free conditions. All experiments were performed in accordance with Swiss Federal Animal Regulations and approved by the Veterinary Office of Zürich.

3.1.4 Small Animal Radiation Research Platform

All irradiations were performed with the small animal image-guided radiation research platform (X-RAD SmART, Precision X-Ray Inc., Figure 3.1).

X-RAD SmART was operated via Pilot software (Princess Margaret Cancer Center and Precision X-Ray Inc.). Treatment planning was performed in SmART-Plan v.2.0 (MAASTRO Clinic and Precision X-Ray Inc.). Image registration, dose distribution matching and CT-volumetry were performed in the clinical radiation oncology software MIM (MIM Software Inc.).

See also Section 1.4.

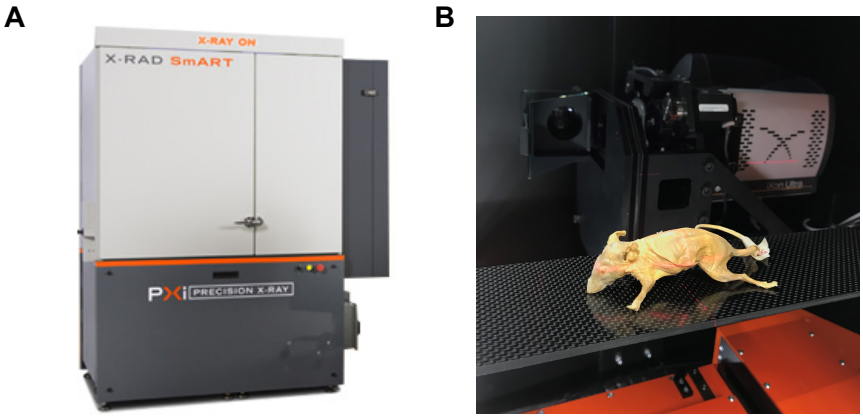

Figure 3.1: **Small animal radiation research platform.** A: X-RAD SmART irradiator B: PlastiMouse plasticized mouse specimen (Precision X-Ray Inc.) on the treatment couch.

3.2 Methods

3.2.1 Dosimetry

Relative dosimetry was performed with Gafchromic EBT3 film which is a self-developing dosimetry film. The film was divided in two parts (Figure 3.2). The first part was used for the film calibration. This was performed by irradiating five film strips with the dose ranging from 0 to 5 Gy using a clinical linear accelerator. A function was used to convert optical density to dose (Figure 3.3). The second part was used to test the dose delivery by X-RAD SmART/SmART-Plan platform and to determine the optimal field arrangement for animal irradiation.

Figure 3.2: **Relative dosimetry performed with Gafchromic EBT3.** The film is divided in two parts. On the left, seven 8 x 12 mm fields are applied such that the distance between the isocenters is, from left to right, 10 mm, 6 mm, 9 mm, 7 mm and 8 mm. On the right, five film strips are irradiated with dose ranging from 0 to 5 Gy (right to left) and used to generate a calibration curve.

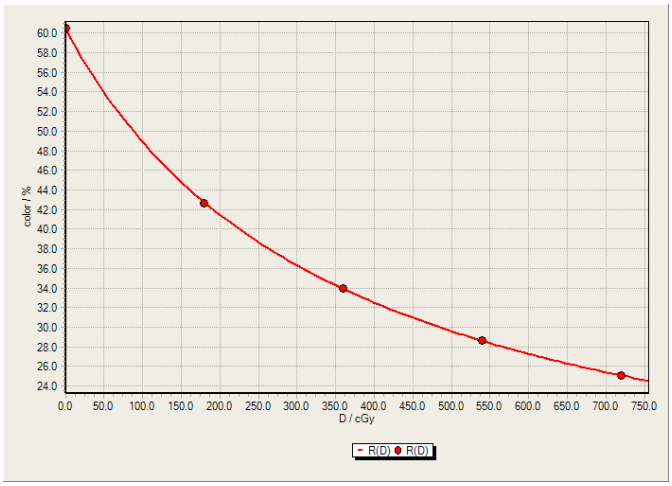

Figure 3.3: **The function for conversion from optical density to dose.** Five film strips were irradiated with dose ranging from 0 to 5 Gy to obtain the calibration curve for relative dosimetry.

3.2.2 Cell Culture

Murine colorectal cancer cell line MC38, a kind gift from Prof. Becher (Institute of Experimental Immunology, University of Zürich), were cultured in DMEM supplemented with L-glutamine, 10% FBS and 1% penicillin/streptomycin at 37°C and 5% CO_2. The cells have tested negative for mycoplasma.

3.2.3 Cell Irradiation and Staining

MC38 cells at 70-80% confluence were irradiated either with a single or six 8 x 12 mm fields, with isocenters set apart 6 mm, 7 mm, 8 mm, 9 mm and 10 mm. Each field delivered 12 Gy. The cells were then incubated for three days post irradiation, fixed with MeOH:HAc and stained with crystal violet.

3.2.4 Subcutaneous Xenografts

MC38 cells in the exponential growth phase were resuspended in ice cold PBS such that there are approximately 3.3 million cells/mL. 150 µL (approximately 500 000 cells) were subcutaneously injected on the back of eight week old female C57Bl/6J mice. The mice were kept under isoflurane anesthesia during the procedure.

3.2.5 Radiotherapy

Starting tumor volumes were determined by caliper measurements, according to the formula:

$$V_{tumor} = \frac{W^2 * L}{2} \tag{3.1}$$

where W is the width and L is the length of the tumor. Upon reaching the tumor volume of 300 mm^3 ± 10%, animals were assigned to one of the four treatment groups, such that the groups were filled successively. The first mouse to reach a tumor volume of 300 mm^3 was assigned to the first group, the second mouse to the second group etc. The mice were kept under isoflurane anesthesia during all procedures and allowed to recover on a warming pad in a separate cage until completely conscious after irradiation. The irradiation time was adjusted in each treatment such that the median dose to the target volume corresponds to the prescribed dose. The 8 x 12 mm

lead collimator was used to deliver the dose in two opposing lateral fields.

The "No IR" group was sham irradiated. The "Half IR" group received a partial, half-tumor irradiation delivering 12 Gy to the cranial half of the tumor. The spatiotemporal ("STF IR") group received two partial irradiations separated by 24 hours, delivering 12 Gy each. The first irradiation covered the cranial half of the tumor. The field of the second irradiation was positioned such that it covers the caudal half of the tumor and is adjacent to the 25% isodose line of the first irradiation matched to the new CT. The "Full IR" group received two partial irradiations delivering 12 Gy each as in the "STF IR" group, but applied successively. The first irradiation covered the cranial half of the tumor and the second irradiation covered the caudal half. The animal was then allowed to regain consciousness and recover body temperature on a warming pad, followed by the second irradiation as in the "STF IR" group.

See also Appendix B.

3.2.6 Tumor Growth Delay

Tumor volumes were determined daily by caliper according to Equation 3.1 and on days 0, 1, 4 and 7 post irradiation by CT-volumetry in MIM. The mice were kept under isoflurane anesthesia for all measurements. All animals were euthanized on day 7 post irradiation.

3.2.7 Immunohistochemistry

Tumors excised at 30 minutes, 24 hours or 7 days post irradiation were fixed in formalin and embedded in paraffin. Immunohistological endpoints were analyzed on 5 µm thick tumor slices for hematoxyline & eosine (H&E), carbonic anhydrase isozyme IX (CAIX, 1:6000, Abcam, ab184006), CD31 (1:50, Abcam, ab28364), γ-H2AX (1:1000, Cell Signaling, 20E3) and CD4 (1:500, eBioscience, Clone 4SM95). All analysis was performed in QuPath v.0.1.2 (Queen's University Belfast). Semiautomatic "Positive cell detection" tool was adjusted to count the proportion of positive cells in the total area of the tumor slice.

3.2.8 Statistical Analysis

Statistical analysis was performed using GraphPad Prism v.7.0. Tumor growth delay was analyzed by evaluating area under the tumor volume curve (AUC) and the final volume by one-way ANOVA with Tukey's multiple comparisons test. Caliper- versus CT-based volumetry were compared using the paired Student's t-test for the initial volume and one-way ANOVA with Sidak's multiple comparisons test for AUC and the final volume of the relative tumor growth curve (normalized to the corresponding initial volume). Immunohistological data were analyzed by one-way ANOVA with Tukey's multiple comparisons test. For all experiments data are represented as mean ± SD, * = $P<0.05$, ** = $P<0.01$ and *** = $P<0.001$.

Chapter 4

Results

4.1 Development of the Pipeline for Partial Tumor Irradiation

4.1.1 Characterization and Verification of Dose Distribution

The X-RAD SmART/SmART Plan system used in this thesis was commissioned in February 2016 whereby an excellent agreement was found between radiochromic film measurements and SmART-Plan calculated dose distributions. The collimator chosen for this study according to the expected tumor size was the R8-12 (dimensions 8 x 12 mm). According to the commissioning report, for this collimator the dose distribution in the isocenter was characterized as follows (Supplemental Figure A.1):

- 0.6% difference was found between the mean dose measured by the radiochromic film (RCF) and SmART-Plan simulated dose, where the mean dose is measured in the region of interest between 80% $dose_{max}$ and 100% $dose_{max}$

- the penumbra (distance between 80% $dose_{max}$ and 100% $dose_{max}$) was 0.9 - 1.0 mm in both the lateral and longitudinal profiles according to RCF and 0.5 - 0.7 mm according to SP

As the first part of this subproject, an RCF dosimetry was undertaken to confirm the results of the commissioning (Figure 4.1).

The results were as follows:

- 0.1% difference was found between the mean dose measured by the RCF and SmART-Plan simulated dose (1.97 and 1.96 Gy for the lateral and longitudinal direction, respectively, versus 2.00 Gy for SP)

- the penumbra was 0.4 - 0.5 mm

Additionally, a "biodosimetric" procedure was performed by irradiating mouse colon cancer cells (MC38) with the R8-12 collimator to determine the sharpness of the dose distribution and dimensions of the field on the biological level (Figure 4.2). In response to 12 Gy, the approximately 8 x 12 mm sized field was easily visualized 3 days post irradiation as the area with almost no viable cells. Repopulation was observable at the edges of the field.

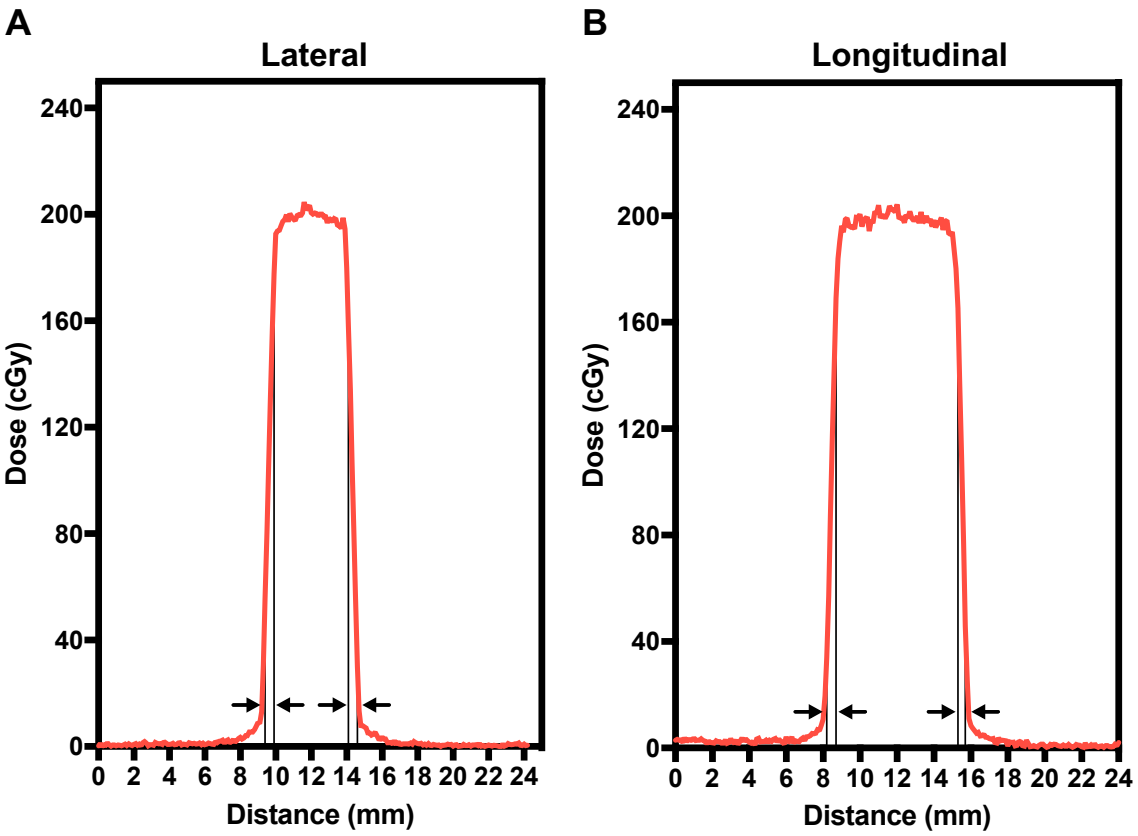

Figure 4.1: **Dose profiles of the R8-12 collimator.** A: Lateral dose profile. The mean dose is 198 cGy, the penumbra (indicated by vertical bars and arrows pointing towards each other) is 0.5 mm on each side. B: Longitudinal dose profile. The mean dose is 197 cGy, the penumbra (indicated by vertical bars and arrows pointing towards each other) is 0.5 mm on the left and 0.4 mm on the right.

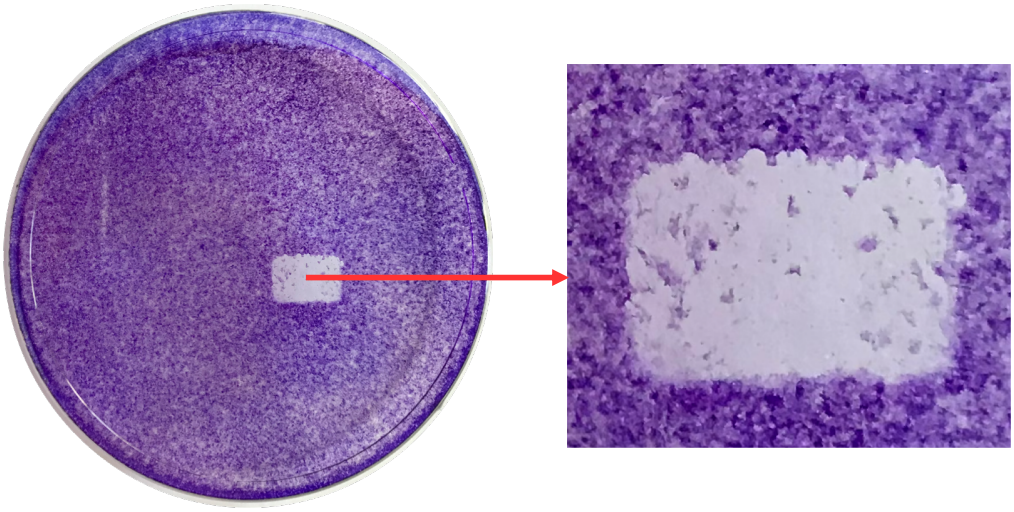

Figure 4.2: **Characterization of the R8-12 collimator on the biological level.** MC38 cells were irradiated with 12 Gy and fixed 3 days post irradiation. The 8 x 12 mm sized field is easily visualized as the transparent area (no viable cells) as opposed to the densely populated surrounding area where living cells are stained with crystal violet.

4.1.2 Optimization of Treatment Planning Workflow

A general SmART-Plan workflow is summarized in Figure 1.8. For partial subcutaneous tumor irradiation in the context of this thesis, the CT2MD step modification was proposed whereby a five-tissue rather than a four-tissue segmentation process is implemented to increase the accuracy of the planning procedure [59]. In the Contouring step, only the tissue to be irradiated was to be delineated, as the dose to the normal tissue was not an endpoint being considered. The goal of the subsequent Beams step is to define the field size and beam number and directions. To increase dose homogeneity and avoid normal tissue toxicity (primarily gastrointestinal side effects [60, 61]), two opposing lateral 8 x 12 mm fields were found to be most suitable (Figure 4.3).

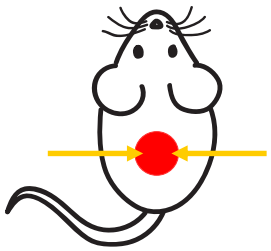

Figure 4.3: **Irradiation scheme for partial subcutaneous tumor treatment.** Two opposing lateral beams (in yellow) are placed such that the tumor (in red) is fully accessible and the underlying normal tissue is spared.

By default, SmART-Plan treats the prescribed dose as the dose to the isocenter. This corresponds to The International Commission on Radiation Units and Measurements (ICRU) Reference Point (based on ICRU report 62 [62]), a widely accepted concept still used in the clinics. The reference point (isocenter in SmART-Plan) should be placed in the representative area of the target. Due to software limitations, and depending on the target geometry, this is often not possible. It is therefore suggested that the prescribed dose should correspond to the median dose in the target volume, based on the ICRU approved approach (ICRU report 83 [63]). To convert the prescribed dose into the median dose, a dose-volume histogram (DVH) is first generated with the prescribed dose given to the isocenter, followed by an adjustment in the irradiation time according to the simulated median dose. For example, 12 Gy prescribed to the isocenter can result in a median dose of 11 Gy to the target with an irradiation time of 240 seconds. Here, the irradiation time is adjusted to 240 * (12/11) = 261 seconds.

4.1.3 Image Registration to Account for Interfractional Movement

Image registration is the process in which two or more images of the same area of interest taken at different times are overlayed and geometrically aligned [64]. It is a necessary step in fractionated radiotherapy as the patient inevitably moves in the time between fractions. In this thesis, subcutaneous tumors underwent fractionated treatment whereby one half of the tumor was irradiated in the first fraction and the other half was irradiated 24 hours later in the second fraction. To achieve this, it was necessary to align the image taken on the second day with the original image and the accompanying dose distribution.

X-RAD SmART/SmART-Plan system offers a simple image matching procedure via the Pilot software where it is possible to move the couch such that the current image partially aligns to the previous image. This procedure only allows translational movement and no rotation due to mechanical limitations and is therefore not applicable when the subject is rotated or there is tissue deformation. Additionally, dose distribution and structure import are not supported.

To overcome these issues, data was imported and processed in MIM, a clinical radiation oncology software. For the purpose of this study, a rigid registration was proposed, which includes translations and rotations of one image onto another. Deformable image registration may offer advantages when notable soft tissue deformations are expected, such as with physiological changes (bladder and stomach filling) and disease- or treatment-related effects (weight loss, tumor shrinkage) [65]. None of these were found significant for subcutaneous tumor models subject to two or fewer fractions, as used in this thesis.

4.1.4 Optimization of Fractionated Dose Homogeneity

As described above, MIM was used to perform image registration. To be able to compare a tumor fully irradiated in one day with a tumor irradiated by two partial irradiations (each covering exactly one half of the tumor), it was necessary to align the two fields such that the resulting dose distribution is as homogeneous as possible. The initial investigation included six 8 x 12 mm fields positioned such that the distance between isocenters was 6 mm (2 mm overlap), 7 mm (1 mm overlap), 8 mm (adjacent fields), 9 mm (1 mm apart) and 10 mm (2 mm apart) (Figure 4.4). Both a cell culture and dosimetric film were irradiated with 12 Gy and 2 Gy, respectively, to enable the analysis of different field positioning on both the biological and physical level. Visual inspection clearly showed that the "adjacent fields" i.e. 8 mm between isocenters provided the most homogeneous dose distribution. The result was confirmed with film dosimetry (Figure 4.5).

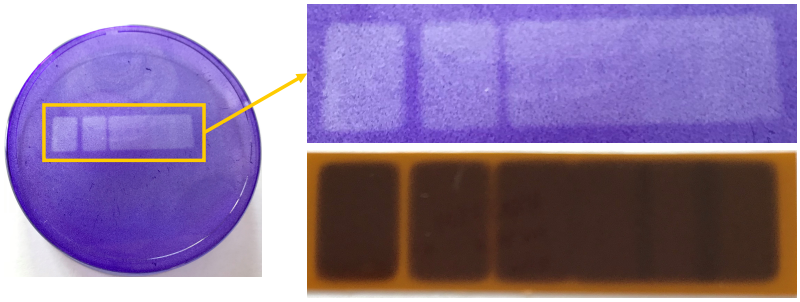

Figure 4.4: **Influence of field positioning on the homogeneity of dose distribution.** Six 8 x 12 mm fields are positioned such that the distance between isocenters is 10 mm, 9 mm, 8 mm, 7 mm and 6 mm, making the distance between the two neighbouring fields 2 mm, 1 mm, 0 mm, -1 mm and -2 mm (i.e. 1 mm and 2 mm overlap), respectively (left to right). In the upper box, MC38 cells were irradiated with 12 Gy and stained with crystal violet 3 days post irradiation. Lightly stained rectangles correspond to irradiation fields. In the lower box, RCF was irradiated with 2 Gy. Color change is proportional to the absorbed dose. Visual inspection suggest that the adjacent fields (8 mm apart) provide the most homogenous dose distribution. A 1 mm overlap (7 mm distance) is clearly visible as an area of increased dose deposition in the RCF.

The 8 mm isocenter spacing was determined to be the optimal solution for field positioning when two field are applied simultaneously by using SmART-Plan. However, in order to irradiate the tumor with two fractions given 24 hours apart, as was done in this thesis, it was necessary to perform an additional image registration step via MIM. Since it is not possible to transfer the treatment plan or the isocenter from SmART-Plan into MIM, it was necessary to find an alternative. Considering it is possible to register an old dose distribution to the new image in MIM, a suitable solution was to use the best fitting isodose line (ISL), transform it into a structure (a format supported by SmART-Plan) and align the field of the second irradiation with the ISL.

To determine the most suitable ISL, the dose homogeneity was tested by aligning the second field to the 15%, 25% and 50% ISL of the original field (Figure 4.5). A visual inspection already suggested the 25% ISL as the most suitable solution, which was confirmed by comparing the ho-

mogeneity index (HI), defined here as the difference between $dose_{max}$ and $dose_{min}$ in the inner half of the irradiated area. The HI was measured to be 30, 15, and 30 cGy for 15%, 25% and 50% ISL matching, respectively.

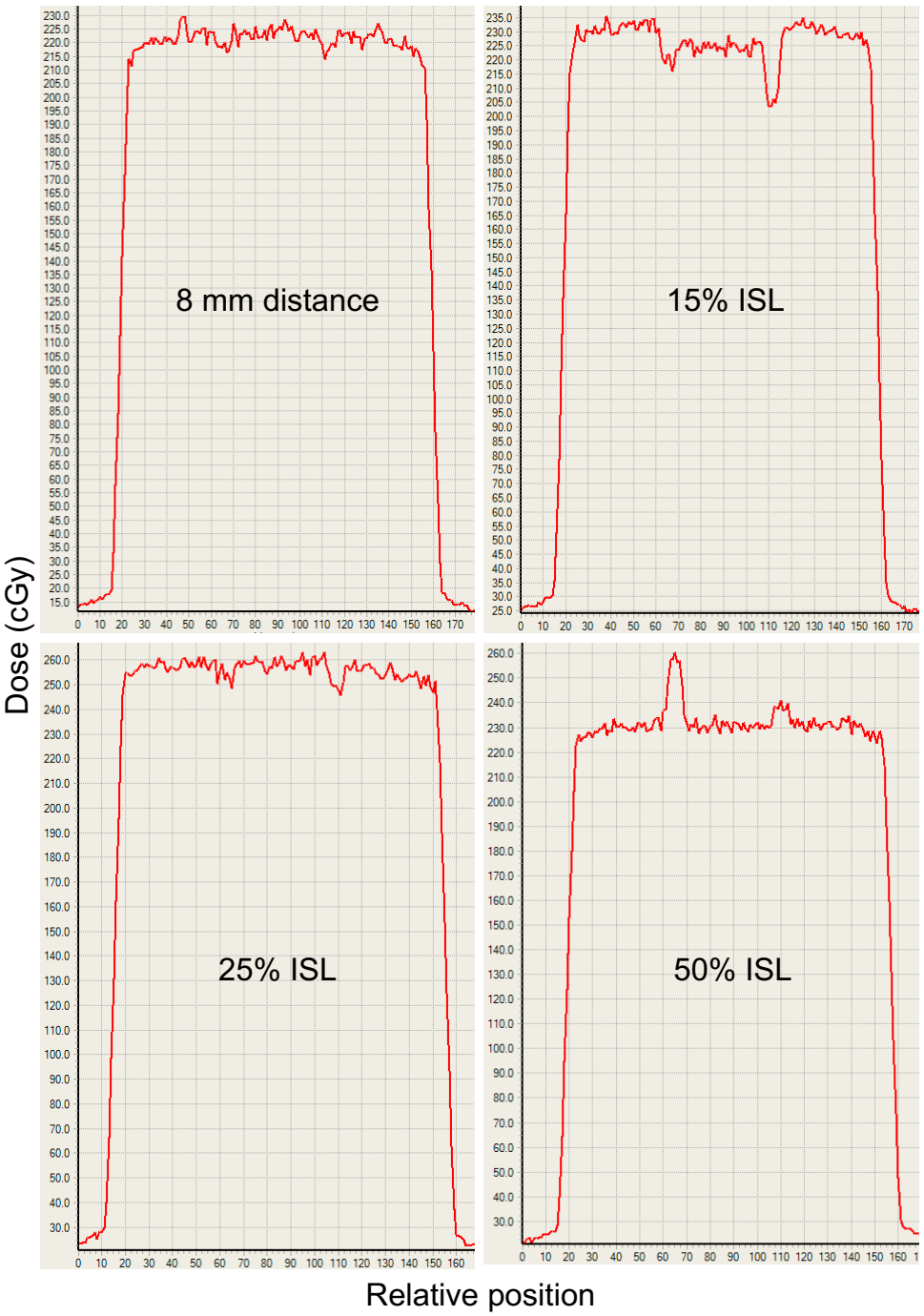

Figure 4.5: **Dosimetric analysis of field positioning.** RCF was irradiated with three 8 x 12 mm fields positioned such that the isocenters were 8 mm apart (top left) or the second field matched the 15%, 25% or 50% ISL of the first field (top right, bottom left and bottom right, respectively). The 25% ISL matching shows the highest resemblance to the adjacent fields. The homogeneity index is 15 cGy for adjacent and 25% ISL matching and 30 cGy for 15% and 50% ISL matching.

4.1.5 CT-Based Volumetry for Longitudinal Studies

One of the endpoints considered in this thesis was the tumor growth delay. The most commonly used method for volume determination in this type of longitudinal studies is external caliper measurement. This is done by measuring the longest dimension of the tumor (length, L) and the diameter perpendicular to length (width, W) (Figure 4.6). The modified ellipsoidal formula is then applied as follows [66, 67]:

$$V_{tumor} = \frac{L * W^2}{2} \tag{4.1}$$

However, caliper-based measurements are inherently prone to errors due to variability in tumor shape (Equation 3.1 assumes an ellipsoid) and thickness of the skin and subcutaneous fat. Therefore, in this thesis, in addition to daily caliper measurements, CT-based volumetry was performed to determine tumor volumes.

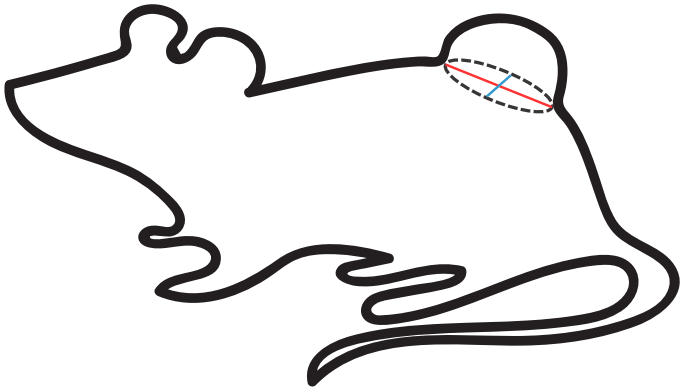

Figure 4.6: **External caliper measurement of tumor volume based on the modified ellipsoidal formula.** Length is defined as the longest dimension (in red) and width is perpendicular to the length (blue). The formula assumes that the tumor is an ellipsoid and the protruding part is equal in size to the width.

Prior to volumetry, a dosimetric study was undertaken to estimate the dose absorbed by the mouse during each imaging procedure (Table 4.1). The "Soft Tissue Mid Dose" preset was found the most appropriate in the context of this thesis, with the total dose per scan amounting to 1.3 (Scout CT) + 4.5 (Soft Tissue Mid Dose) = 5.8 cGy. According to recent studies [53, 68], a whole-body dose of up to 10 cGy is safe for repeated CT imaging in longitudinal mouse studies, thereby confirming the usability of "Soft Tissue Mid Dose" protocol for this thesis.

Table 4.1: **X-RAD SmART CT imaging dosimetry.** Scout CT is an initial image taken to position the isocenter by adjusting the treatment couch. "Soft Tissue Low/Mid/High Dose" are the presets intended for imaging soft tissues in mice with low, middle and high resolution, respectively.

Scout CT	1.3 cGy
Soft Tissue Low Dose	2.3 cGy
Soft Tissue Mid Dose	4.5 cGy
Soft Tissue High Dose	11.9 cGy

4.1.6 Validation of the Pipeline

To conclude this subproject, a validation study was performed, first on a wooden phantom (Figures 4.7, 4.8 and 4.9), and then by irradiating a tumor-bearing mouse (Figures 4.10 and 4.11). The complete pipeline (Appendix B) for fractionated partial tumor irradiation, whereby each fraction irradiates exactly one half of the tumor, resulted in a homogenous dose distribution in the target.

Figure 4.7: **Validation of the pipeline on the wooden phantom.** The target was treated in two fractions, each covering one half of the tumor. Two 8 x 12 mm fields were positioned such that the second field is aligned to the 25% ISL of the dose distribution produced by the first field. The resulting dose deposition is visible as the dark area on the orange RCF.

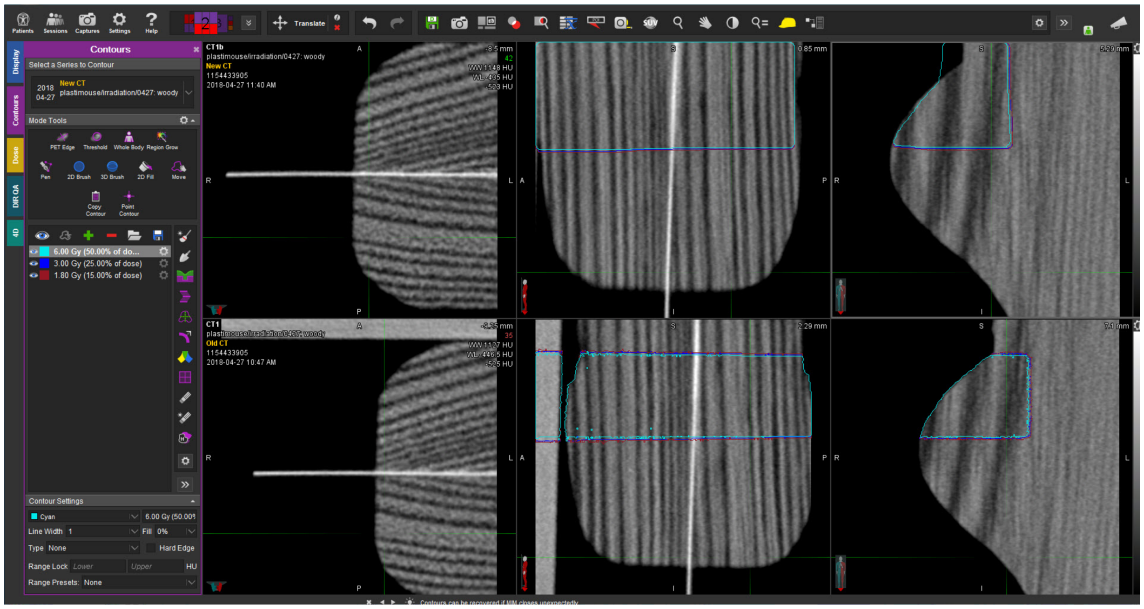

Figure 4.8: **Image matching for the wooden phantom in MIM.** The 15%, 25% and 50% ISL from the first fraction are converted into contours and shown on the old CT in the bottom row. The top row shows the new CT with ISL contours matched to the new position.

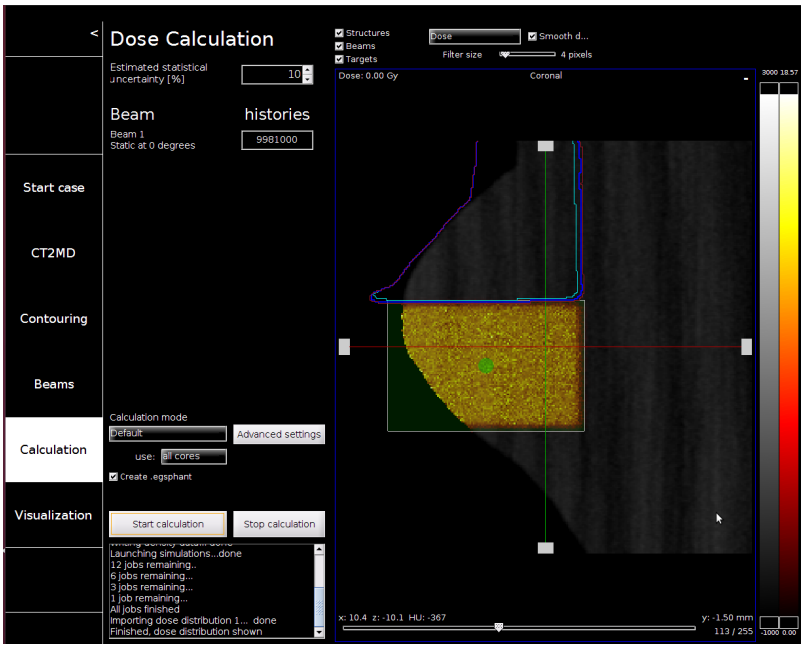

Figure 4.9: **Planning the second half-tumor treatment in the wooden phantom according the the matched dose distribution of the first fraction.** Red, dark blue and light blue lines correspond to 15%, 25% and 50% ISL, respectively. The field of the second fraction (green area) is aligned with the 25% ISL of the first fraction. The green dot is the isocenter and the colored area represents the calculated dose distribution for the second fraction.

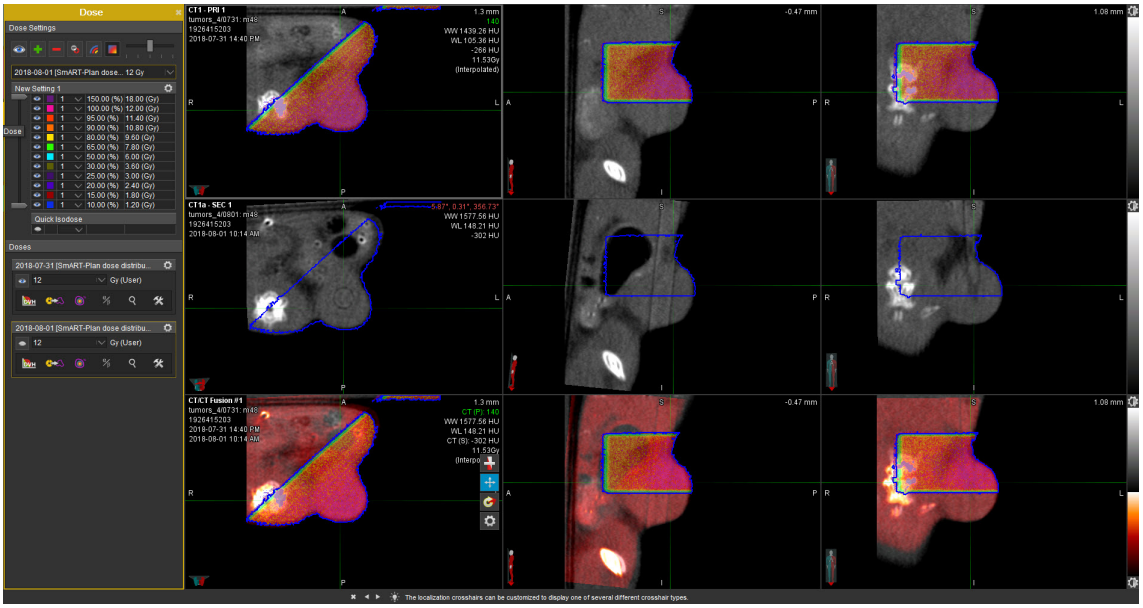

Figure 4.10: **Image matching for the tumor-bearing mouse in MIM.** The top row shows the old CT image with dose distribution of the first fraction and the 25% ISL highlighted in blue. The middle row shows the new CT image with the 25% ISL from the first fraction matched to the new CT. The bottom row shows overlayed CT images and the dose distribution of the first fraction.

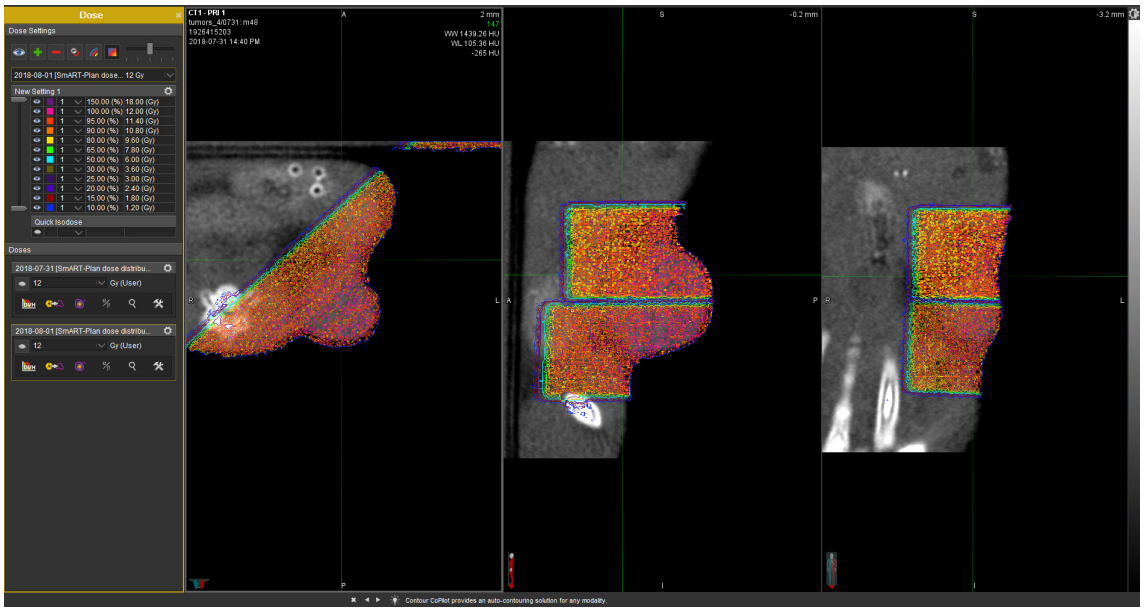

Figure 4.11: **Final dose distribution in the tumor-bearing mouse treated with two partial irradiations.** Cranial part or the tumor (up in the figure) was treated with the first partial irradiation and the caudal part of the tumor (down in the figure) was treated with the second partial irradiation. The two irradiations were aligned such that the 25% ISL of the first irradiation matches the edge of the field of the second irradiation. The resulting dose distribution from both irradiations is shown on the CT taken at the time of the second irradiation.

4.1.7 Conclusion

Overall, this subproject resulted in the development of a novel pipeline for partial tumor irradiation in experimental animal models. For the first time, the X-RAD SmART/SmART-Plan system treatment planning is extended to the clinical software MIM to allow for image registration and thus fractionated, partial- or complete-volume radiotherapy in small animals.

4.2 Influence of Spatiotemporal Fractionation on the Tumor Growth Delay

4.2.1 Tumor Growth Delay

To investigate spatiotemporal fractionation (STF) in an experimental tumor model, xenografts derived from MC38 cells were treated with two partial irradiations (each covering exactly one half of the tumor) separated by 24 hours ("STF IR" group). The tumor growth delay of the "STF IR" group was compared to the growth delay of either fully ("Full IR" group) or partially ("Half IR" group) irradiated tumors (Figure 4.12).

Upon reaching the tumor volume of 300 mm^3 $\pm$ 10%, as determined by caliper, animals were assigned to one of the four treatment groups, such that the groups were filled successively. The first mouse to reach a tumor volume of 300 mm^3 was assigned to the first group, the second mouse to the second group etc. By doing so, each treatment group consisted of an equal number of animals. At the same time, tumors growing at different growth rates were distributed evenly across the groups. The predeveloped X-RAD SmART/SmART-Plan pipeline (Section 4.1, Appendix B) was thereafter used to deliver 12 Gy in each irradiation. Volume measurements were taken daily by caliper until day 7 post irradiation when the mice were euthanized.

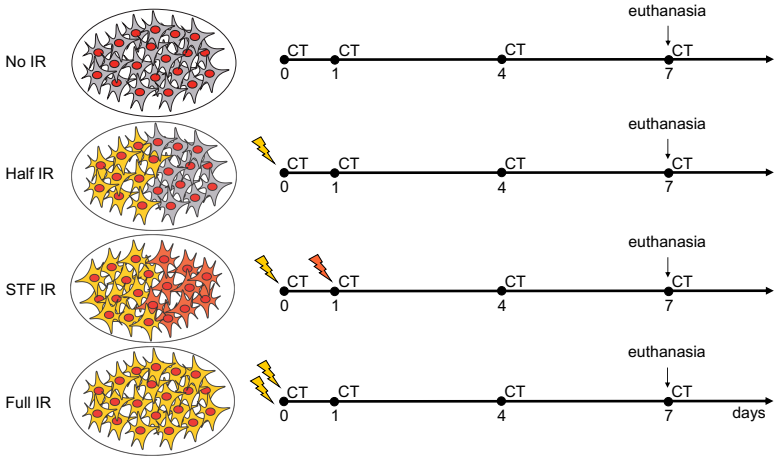

Figure 4.12: **Treatment schedule for the tumor growth delay study.** Upon reaching the tumor volume of 300 mm^3 ± 10%, animals were assigned to one of the four treatment groups, as described in the text. The "No IR" group was sham irradiated. The "Half IR" group was irradiated with a partial irradiation delivering 12 Gy and covering the cranial half of the tumor. The "STF IR" group received two partial irradiations, each delivering 12 Gy, given on day 0 and day 1 and covering the cranial and caudal half of the tumor, respectively. The "Full IR" group received two partial irradiations, each delivering 12 Gy as in the "STF IR" group, but given successively on day 0. All animals underwent CT imaging on days 0, 1, 4 and 7 post irradiation and were euthanized on day 7.

The area under the tumor growth curve (AUC) in the "STF IR" group did not significantly differ from the tumors treated fully ("STF IR" 2060±204 vs "Full IR" 2095±343). Furthermore, absolute tumor volume at day 7 post irradiation was not significantly different in the "STF IR" group compared to the "Full IR" group ("STF IR" 244±38mm^3 vs "Full IR" 253±105mm^3). Partially irradiated xenografts ("Half IR" group) followed a growth curve significantly different from both the unirradiated control ($P<0.01$) and the "STF IR"/"Full IR" groups ($P<0.001$) (Figures 4.13A and 4.14A, Supplementary Table A.1).

These results demonstrate that tumors irradiated to the same dose, either immediately or with a 24 hour delay between two partial irradiations, exhibit no difference in the growth delay study, while a reduction in the irradiated volume results in an intermediate response.

4.2.2 Caliper- versus CT-Based Volumetry

For this tumor growth delay study investigating STF, in addition to daily caliper-based volumetry (CALVM), CT images were taken on days 0, 1, 4 and 7 post irradiation for subsequent CT-based volumetry (CTVM).

CTVM measured overall significantly smaller initial volumes with an increased dispersion compared to CALVM (CTVM 238±53mm^3 vs CALVM 288±14mm^3, $P<0.001$). Therefore, prior to the analysis of growth rate, the data was normalized to the corresponding initial volume, yielding a relative tumor growth curve.

Equivalent to CALVM, AUC in the "STF IR" group did not significantly differ from tumors treated fully ("STF IR" 6.48±1.52 vs "Full IR" 6.48±0.74). Relative tumor volume at day 7 post irradiation was not significantly different in the "STF IR" group compared to the "Full IR" group ("STF IR" 0.85±0.12 vs "Full IR" 0.79±0.31). Partially irradiated xenografts ("Half IR" group) followed a growth curve significantly different from both the unirradiated control ($P<0.01$) and

the "STF IR"/"Full IR" groups (P<0.001) (Figures 4.13B and 4.14B, Supplementary Table A.1).

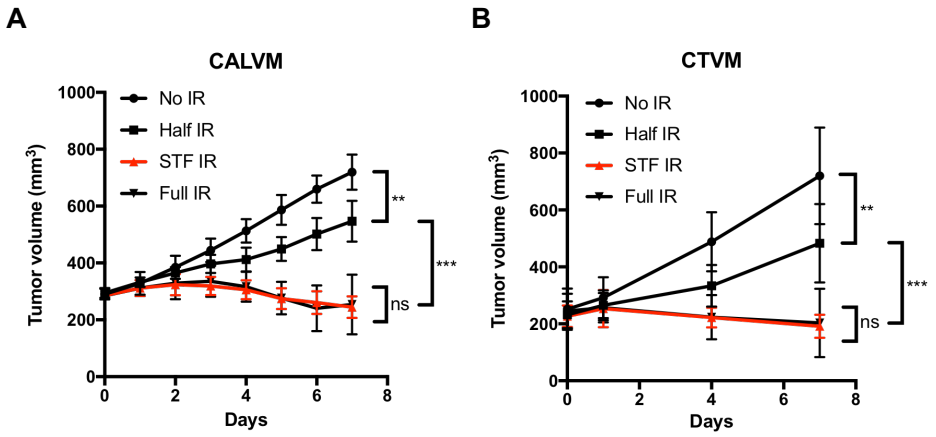

Figure 4.13: **Treatment response determined by caliper- and CT-based volumetry.** A: Caliper-based tumor growth curves. B: CT-based tumor growth curves. No significant differences in the final volume or the area under the tumor growth curve are found between the "STF IR" and the "Full IR" groups. The "Half IR" group is significantly different from both the "STF IR"/"Full IR" and "No IR" groups. Data are represented as mean ± SD, n = 6 for each data point. ns = not significant, ** = P<0.01, *** = P<0.001.

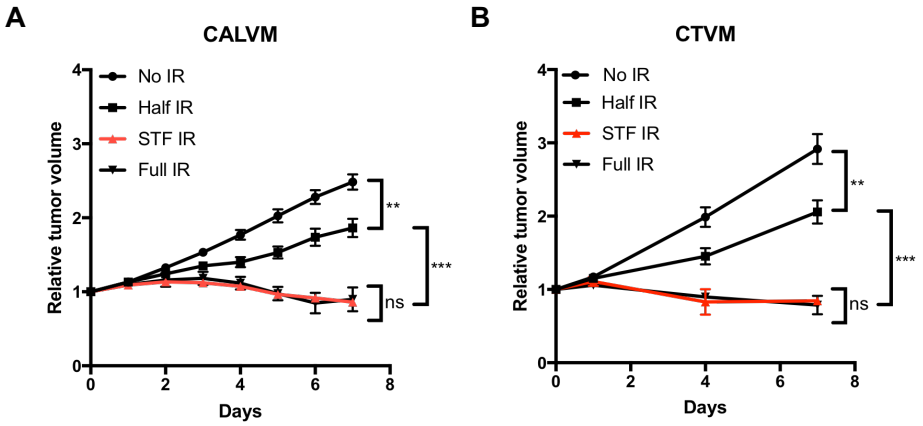

Figure 4.14: **Relative tumor growth curves.** A: Caliper-based tumor growth curves. B: CT-based tumor growth curves. Each point is normalized to the corresponding starting volume. Data are represented as mean ± SD, n = 6 for each data point. ns = not significant, ** = P<0.01, *** = P<0.001.

Further direct comparison of CTVM versus CALVM by analyzing the relative tumor growth (defined as the final volume divided by the initial volume) and AUC for the relative tumor growth curve showed no significant differences between the two methods. Following an analysis of individual tumor growth curves, an outlier was identified in the Half IR group according to CTVM, but not CALVM (Figure A.2). Since CALVM is used as the basis in this thesis, the outlier has not been excluded from any of the results presented here.

The results obtained by CTVM support the findings of the caliper-based tumor growth investigation. Although the initial volumes determined by CTVM were on average smaller and more

dispersed, this did not affect the relative tumor growth measurements, suggesting the two methods to be interchangeable for relative, but not absolute measurements.

4.2.3 Conclusion

Overall, this tumor growth study supports the assumption of STF that the tumor response can be predicted by locally adding up biological doses from each fraction in a reductionistic preclinical model of STF, as determined by both caliper- and CT-based measurements. Furthermore, comparison of the two methods suggests caliper and CT to be interchangeable when relative tumor growth is an endpoint.

4.3 Effects of Spatiotemporal Fractionation on the Histological Level

4.3.1 Induction of Double-Strand DNA Breaks: γ-H2AX

To investigate the effects of STF on the level of the double-strand DNA break (DSB) induction, xenografts derived from MC38 cells were treated with two partial irradiations (each covering exactly one half of the tumor) separated by 24 hours ("STF IR" group). The mice were subsequently euthanized 30 minutes after the second irradiation, corresponding to 24 hours after the first irradiation. The proportion of cells positive for the DSB marker γ-H2AX (Section 1.2.2) in the two distinct halves of the "STF IR" group, either irradiated 24 hours or 30 minutes prior to euthanasia, was compared to both fully ("Full IR" group) and partially ("Half IR" group) irradiated tumors, treated either 24 hours and 30 minutes prior to euthanasia (Figure 4.15).

Animals were assigned to experimental groups upon reaching the tumor volume of 300 mm^3 $\pm$ 10% (determined by caliper) by filling the groups successively, as described in the previous section. The predeveloped X-RAD SmART/SmART-Plan pipeline (Section 4.1, Appendix B) was thereafter used to deliver 12 Gy in each irradiation. Animals were euthanized and tumors excised either 30 minutes or 24 hours post irradiation.

Tumor tissues fixed at 30 minutes post irradiation and compared in this study included the fully irradiated tumors ("Full30"), the irradiated half of the partially irradiated tumors ("Half30") and the half of the "STF IR" group tumors treated with the second partial irradiation ("STF30"). In the tumor tissue irradiated with the second partial irradiation in the "STF IR" group ("STF30"), the proportion of cells positive for γ-H2AX was significantly lower compared to the "Half30" and "Full30" groups ("STF30" 29.1$\pm$4.5% vs "Half30" 46.1$\pm$12.9% and "Full30" 40.3$\pm$7.3%, $P<0.001$ and $P<0.01$, respectively) (Figures 4.16 and 4.17, Supplemental Table A.2). There were no significant differences detected in the proportion of γ-H2AX positive cells at 30 min post irradiation between the irradiated half of the partially irradiated tumors ("Half30") and the fully irradiated tumors ("Full30").

In the tumor tissues fixed at 24 hours post irradiation, there were no significant differences found between the fully irradiated tumors ("Full24"), the irradiated half of the partially irradiated tumors ("Half24") and the half of the "STF IR" group tumors treated with the first partial irradiation ("STF24"). Furthermore, no significant differences were found between the tumor tissues that received no irradiation, which included the sham-irradiated tumors ("No IR") and the non irradiated half of the partially irradiated tumors, fixed either at 30 minutes ("Half30 -") or 24 hours ("Half24 -") post irradiation (Figures 4.16 and 4.17).

These results show that, in tumors that received the first partial irradiation 24 hours prior to the second partial irradiation, there is a decrease in the incidence of DSBs in cells covered by the second irradiation. The discrepancy found here between the "STF IR" group and "Full IR" group

suggests possible differences on the level of the initial DNA damage in response to partial tumor irradiation.

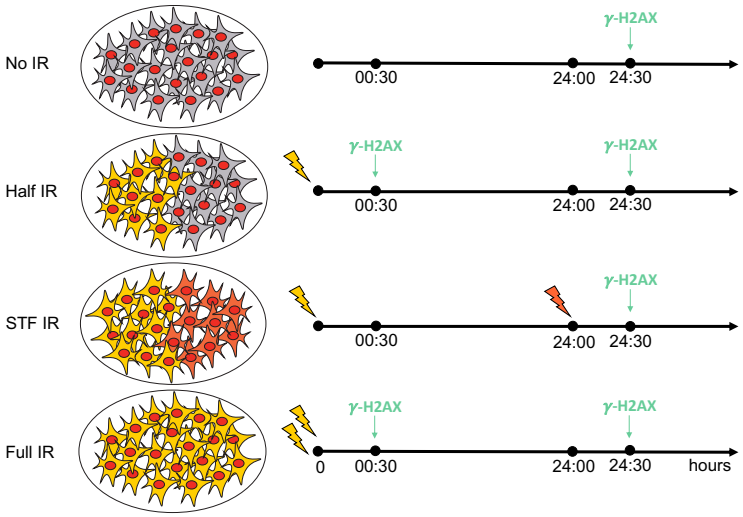

Figure 4.15: **Treatment schedule for the γ-H2AX study.** The "No IR" group was sham irradiated. The "Half IR" group was irradiated with a partial irradiation delivering 12 Gy and covering the cranial half of the tumor. The "STF IR" group received two partial irradiations separated by 24 hours, delivering 12 Gy each. The "Full IR" group received two partial irradiations, delivering 12 Gy each as in the "STF IR" group, but applied successively. Animals were euthanized and tumors excised either 30 minutes or 24 hours post irradiation.

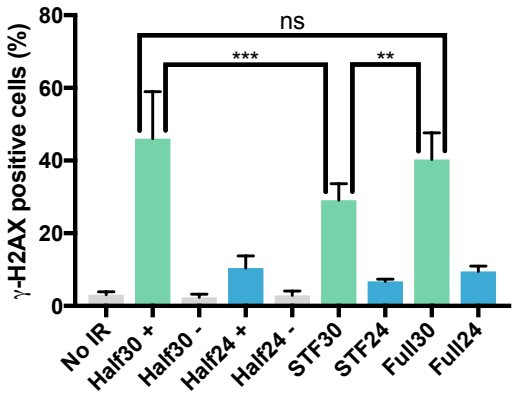

Figure 4.16: **Influence of spatiotemporal fractionation on the proportion of γ-H2AX positive cells.** In the "Half IR" and the "Full IR" groups, tumors were excised either 30 minutes ("Half30", "Full 30") or 24 hours ("Half24", "Full24") post irradiation. The irradiated half is denoted by (+) and the non irradiated by (-). In the "STF IR", the tumor was excised 30 minutes post second irradiation and 24 hours post first irradiation. The respective halves of the tumor are denoted "STF30" (second irradiation) and "STF24" (first irradiation). Green columns represent cells irradiated 30 minutes prior to analysis and blue columns represent cells irradiated 24 hours prior to analysis. Grey columns are cells that received no irradiation. Significant differences are found between the "STF30" group compared to both the "Half30" and "Full30" group. Data are represented as mean ± SD, n = 3. ** = $P<0.01$, *** = $P<0.001$.

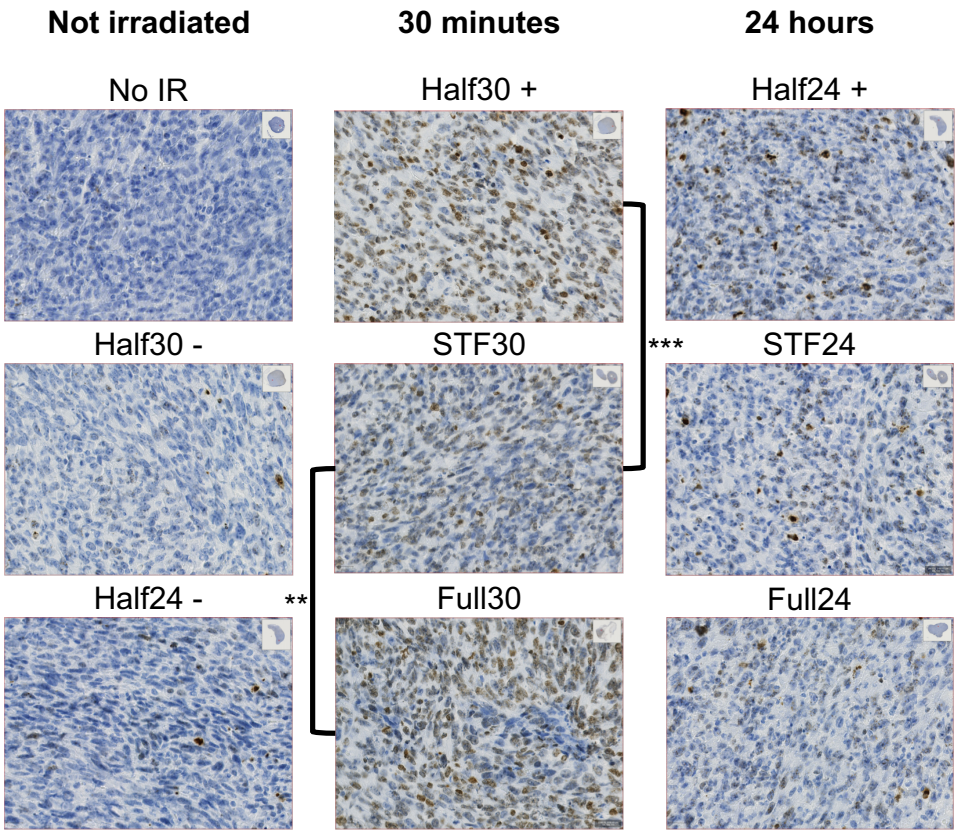

Figure 4.17: **Representative immunohistological slides stained for γ-H2AX.** Left column are the non irradiated cells (the "No IR" group and non irradiated half of the "Half IR" group). Slides in the middle were stained 30 minute post irradiation and slides in the right column were stained 24 hours post irradiation. Significant differences are found between the second irradiation in the "STF IR" group ("STF30") compared to both partially ("Half30") and fully ("Full30") irradiated groups. Blue represents cell nuclei and brown represents γ-H2AX foci. ** = $P<0.01$, *** = $P<0.001$

4.3.2 Microvessel Density

To investigate the effects of STF on the microvessel density, tumors excised on day 7 post irradiation from the tumor growth delay study (Figure 4.12) were analyzed for the presence of the endothelial cell surface antigen CD31 (Section 1.2.2). The automatic detection of the proportion of CD31 positive cells over the whole tumor volume was used as a surrogate marker for the microvessel density. It was assumed that different cuts of the individual vessels, resulting in a different number of CD31 positive cells representing a single vessel, average out over the whole tumor volume and thereby do not affect the results.

In the irradiated half of the "Half IR" group ("Half IR +") there were significantly more CD31 positive cells compared to the non irradiated half ("Half IR -") and the sham-irradiated tumors ("No IR"). Furthermore, the proportion of CD31 cells in the "Half IR +" group was significantly higher compared to both halves of the "STF IR" group tumors ("STF IR d0" and "STF IR d1", corresponding to the part of the tumor irradiated by the first and second partial irradiation, respectively) (Figures 4.18 and 4.19, Supplemental Table A.3). No differences were found between the remaining groups compared to the control or each other.

The data suggests there might be detectable differences in the response of tumors to partial irra-

diation on the level of microvessel density.

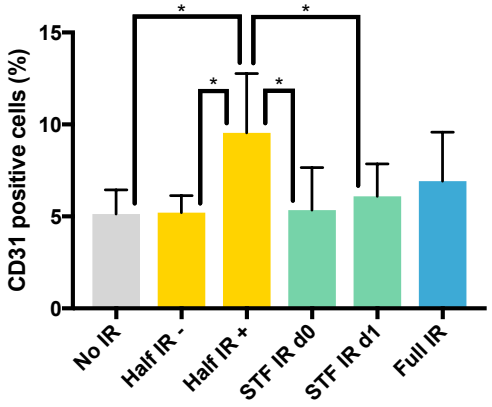

Figure 4.18: **Influence of spatiotemporal fractionation on the microvessel density represented by CD31 staining.** Tumors in the control group were sham irradiated ("No IR", yellow columns, n = 3). In the "Half IR" group (yellow column, n = 2), cranial half of the tumor received 12 Gy ("Half IR +") and the caudal half received no irradiation ("Half IR -"). The "STF IR" group (green columns, n = 4) received two partial irradiations separated by 24 hours, delivering 12 Gy each. The respective halves of the tumor are denoted "STF IR d0" (first irradiation) and "STF IR d1" (second irradiation). The "Full IR" group (blue column, n = 4) received two partial irradiations delivering 12 Gy as in the "STF IR" group, but applied successively. The irradiated half of the "Half IR" has significantly more CD31 positive cells compared to both halves of the "STF IR" group, the non irradiated half of the "Half IR" group and the control. No significant differences are found between other groups. Data are represented as mean ± SD. * = $P<0.05$.

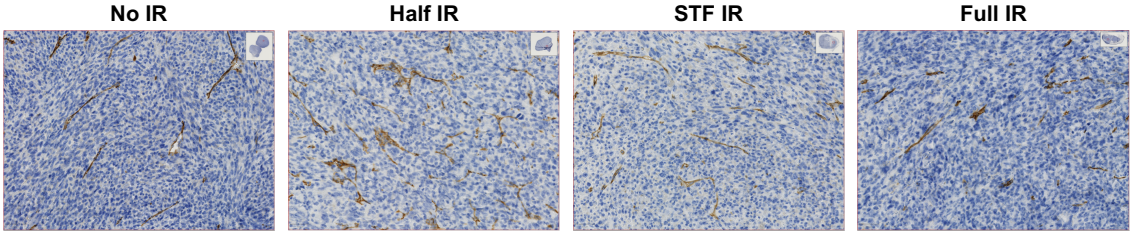

Figure 4.19: **Representative immunohistological slides stained for CD31.** Irradiated half of partially irradiated tumors ("Half IR") are found to have more CD31 positive cells compared to the control ("No IR"), the non irradiated half of partially irradiated tumors (image not shown) and the "STF IR" group. Blue represents cell nuclei and brown represents the CD31 antigen i.e. endothelial cells.

Note: An additional pilot investigation of an immunological endpoint (CD4+ lymphocyte infiltration) and oxygenation status (carbonic anhydrase isozyme IX, CAIX) was undertaken and showed no significant results in the small sample size analyzed.

4.3.3 Conclusion

Overall, this investigation of the effects of STF on the histological level suggests possible differences in the response of tumors to partial irradiation, as shown by changes in the initial DNA damage in cells in contact with preirradiated tissue and changes in the microvascular density in partially irradiated tumors.

Chapter 5

Discussion

In conventional radiotherapy, the treatment is typically fractionated and a uniform dose is delivered in each fraction across the whole tumor volume [62]. The benefits of fractionation were empirically discovered early in the history of radiotherapy [26, 27] and later attributed to a variety of biomolecular differences between the neoplastic and healthy tissue. In his famous report from 1975 [28], Withers proposed the "4 Rs of Radiotherapy" (repair, redistribution, repopulation and reoxygenation) as the four key mechanisms that explain the differential effects of fractionation on the tumor and normal tissue. To improve tumor control, primarily by inhibiting repair and repopulation, a high dose per fraction in combination with a short overall treatment time is required. By doing so, however, normal tissue toxicity is increased. An ideal treatment would therefore increase the therapeutic window by simultaneously achieving hypofractionation in the tumor along with near uniform fractionation in normal tissues. Spatiotemporal fractionation (STF) is a novel approach to achieve these goals [46, 47, 48, 49, 50, 51].

In STF each fraction delivers a high single fraction dose to alternating parts of the tumor while creating a similar dose bath in the surrounding normal tissue. This is achieved by delivering a distinct dose distribution in each fraction, contrary to conventional radiotherapy where all fractions deliver the dose according to the same treatment plan. Previous treatment planning studies demonstrated the benefit of STF *in silico* in the context of cerebral arteriovenous malformations and liver tumors [48, 50]. These studies were based on the working hypothesis that different parts of the tumor can be treated in different fractions, as long as the cumulative biological dose that each part receives corresponds to the prescribed dose. In this thesis, an initial step is taken for the first time towards verifying this assumption in an experimental animal model.

In a reductionistic preclinical model of STF, xenografts treated with two partial irradiations separated by 24 hours and delivering 12 Gy each were compared to conventionally irradiated xenografts, treated with two partial irradiations delivering 12 Gy each as in the test group, but applied successively. This reductionistic model was designed in such a way to avoid dose fractionation and thus the necessity of using the α/β ratio to calculate the relevant biologically effective dose [37, 38], since the determination of this ratio for the cell line used was not a part of this thesis and no reliable data is available in the literature. The model was found to be sufficient for the initial investigation of STF on the preclinical level performed in this thesis. However, an extension is warranted for further studies to include dose fractionation as performed in STF.

First a pipeline was developed to perform such fractionated irradiation of varying target volumes in a small animal model. The pipeline was implemented in a tumor growth delay study, where it was shown that tumors in the STF group exhibit no difference in growth compared to fully irradiated tumors, suggesting the assumption of STF to be valid. Furthermore, an immunohistological study was undertaken to investigate the DNA damage- and tumor microenvironment-related endpoints in the broader context of partial tumor irradiation. Investigation of the initial DNA damage and

microvascular suggests possible differences in the response of tumors to inhomogeneous irradiation.

5.1 Development of the Pipeline for Partial Tumor Irradiation

Small animal radiation research platforms have only recently been introduced in an attempt to bring preclinical radiotherapy research closer to modern human radiotherapy practice [53]. Because no standardized protocols yet exist for partial tumor irradiation in an experimental animal model, it was necessary to develop a protocol to enable such treatment. SmART-Plan v.2.0, used in this thesis, is a dedicated small animal treatment planning system complementary to the X-RAD SmART [57]. It allows the user to design, simulate and execute treatment plans in small animals with certain limitations not typically encountered in the clinics. For example, it does not offer steps necessary for fractionated treatment, primarily image registration and importing dose distribution. To the best of the author's knowledge, partial tumor irradiation has not yet been performed in an experimental animal model, and thereby no feasible solutions were available in the literature to overcome these issues.

In this thesis, it was necessary to find an optimal field arrangement such that a homogenous dose distribution is achieved in tumors treated with two partial irradiations, where each irradiation covers exactly one half of the tumor. In an ideal case, the isocenter/treatment plan of the original irradiation would directly be registered to the second CT, allowing the second field to be exactly adjacent to the first field. To enable image registration, clinical radiation oncology software MIM was used. Since SmART-Plan does not support import of external dose distributions or treatment plans and only accepts external structures, converting the 25% isodose line of the original dose distribution into a contour and using this as a point of alignment for the second field was found to be the most feasible solution.

5.2 Influence of Spatiotemporal Fractionation on the Tumor Growth Rate

As proposed by the assumption of STF, tumors irradiated the same dose, either immediately or with a 24 hour delay between two partial irradiations, exhibited no difference in the growth delay study undertaken in this thesis. Therefore, on a macroscopic level, the assumption of STF is confirmed in this preclinical model. Furthermore, as expected, a reduction of the irradiated volume resulted in a decreased response of the tumor, albeit better than in the sham irradiated control.

In this study, fully irradiated tumors were irradiated with two successive partial irradiations rather than one irradiation covering the whole tumor. This was done in an attempt to minimize the possibility of an imprecise field alignment resulting in a false difference between the STF group and the fully irradiated group. Unintended overlap or spacing in the middle zone of the tumor could have lead to increased cell killing or cell survival, respectively, and by treating both groups with two fields, this potential bias is avoided. This successive delivery, however, lead to an increase in the treatment time for the fully irradiated group (up to 45 minutes versus 15 minutes for a single-field irradiation). Prolonged radiation delivery is a known clinical issue being investigated currently in the context of modern intensity-modulated radiation therapy (IMRT). It is speculated that sublethal damage repair takes place in such a situation, potentially leading to a decreased effect of radiation. On the other hand, simultaneous reoxygenation might counteract this effect [69]. Overall, both clinical and preclinical studies suggest possible detrimental effect of delivery time prolongation and although no conclusive data is available, it is currently strongly advised to keep the treatment time a short as possible [70, 71, 72, 73, 74].

In tumor growth delay studies, tumor volumes are usually determined by external caliper mea-

surements. However, caliper-based measurements (CALVM) are inherently prone to errors due to variability in tumor shape and thickness of the skin and subcutaneous fat. An overestimation of tumor volume was found to be frequent when comparing the caliper-based measurements to CT-volumetry (CTVM). Moreover, studies have found significant differences in independent measurements by different observers for CALVM but not CTVM [75, 76]. To investigate this issue, CTVM was compared to CALVM in this thesis and the results showed no differences in the two methods when considering relative tumor growth curves (normalized to corresponding starting volumes). However, there were significant differences between the measurements of the starting volumes determined by the two methods. Considering the complexity of tumor growth, best described by the Gompertz model [77, 78], it is crucial to initiate treatment at approximately the same growth phase of different tumors. In this study, starting volumes and thereby treatment initiation were determined by CALVM only, although CTVM might be superior in this matter. Furthermore, CTVM was able to identify a clear outlier in one of the experimental groups that was overlooked by CALVM. Although this outlier didn't influence the end results in this study, this finding clearly suggests CTVM to be a superior method of measurement. A additional endpoint of interest, not analyzed in this thesis, would be the interobserver agreement i.e. having independent observers taking CTVM and CALVM and determining how these measurements compare to each other.

5.3 Effects of Spatiotemporal Fractionation on the Histological Level

The investigation of the effects of STF on the histological level in this thesis observed differences in the response of tumors to partial irradiation. This was seen in changes in the initial DNA damage in cells in contact with preirradiated tissue and changes in the microvascular density in partially irradiated tumors.

In tumors that received the first partial irradiation 24 hours prior to the second partial irradiation, there was a decrease in the incidence of double strand DNA breaks (DSB) in cells covered by the second, but not first irradiation. Previous *in vitro* work on the effect of non-uniform irradiation fields on cell survival provided evidence that a distantly deposited dose may influence the survival on non-irradiated cells via "the bystander effect" [79]. Further investigation of the bystander effect in the context of IMRT and non-uniform irradiation showed a range of biological responses suggesting that, depending on the dose and cell type, unexposed cells communicating with irradiated cells may exhibit both an increase and decrease in the survival [74, 80, 81, 82, 83]. In this thesis, spatiotemporal field modulation decreased the incidence of DSB in response to second partial irradiation in cells unexposed during the first partial irradiation. This occurrence might be attributed to the bystander effect. No such change in the incidence of DSB was observed in unaffected cells in partially irradiated tumors nor in the fully irradiated tumors where the two partial irradiations were delivered successively, suggesting the 24 hour delay to be necessary for the development of the bystander response. On the macroscopic level, as determined by the tumor growth rate study, there were no differences between the tumors treated with two partial irradiations, either successively or with a 24 hour delay. These results suggest that, in the context of this study, the bystander effect might only be relevant on the level of the initial DNA damage response.

Additional tumor microenvironment- and immunology-related endpoints were analyzed in this thesis. CD31 or platelet endothelial cell adhesion molecule (PECAM-1) is an endothelial cell surface antigen commonly used to visualize endothelial cells and was used here to quantify the microvascular density in the tumor [25]. An increase in CD31 positive cells at day 7 post irradiation was found in the irradiated half of partially irradiated tumors, suggesting an interplay between the non-irradiated and irradiated areas of the tumor. In previous studies, it was shown that ionizing radiation leads to an overall decrease in the functional microvascular network in the tumor, primarily by decreasing endothelial cell proliferation and promoting cell death [23, 24, 84, 85], although

an induction of ineffective angiogenesis was also suggested [85]. Furthermore, there is evidence that ionizing radiation upregulates expression of CD31 as a part of the post irradiation inflammatory response [23, 24, 86, 87, 88, 89]. Overall, previous studies suggest a complex interplay between the tumor microvessel network and ionizing radiation. Differences found in this thesis might be attributed to the effects of radiation-induced inflammation and previously unexplored interactions between the non-irradiated and irradiated cells in a single tumor entity. Further investigation is warranted, primarily with a larger sample size (presently n = 3) and then with additional endothelial cell (e.g. CD34 [90]) and inflammatory markers, to distinguish between inflammation-induced CD31 expression and real microvessel density and to further investigate tumor microenvironment changes in both the irradiated and non-irradiated parts of the tumor.

In this thesis, an additional pilot investigation of an immunological endpoint (CD4+ lymphocyte infiltration) and oxygenation status (carbonic anhydrase isozyme IX, CAIX) was undertaken and showed no significant results in the small sample size (n = 2) analyzed. A more extensive analysis of immunological and inflammatory endpoints should be undertaken to provide insight into the role of the immune system in the context of partial irradiation. Furthermore, a different marker of the oxygenation status should be probed to enable a more detailed analysis of the oxygenation status of the tumors and possibly correlate these findings to differences on the level of microvessel density and initial DNA damage induction found in this thesis.

Chapter 6

Conclusion

Overall, the assumption of spatiotemporal fractionation that the tumor response can be predicted by locally adding up biological doses from each fraction is supported in this thesis in a reductionistic preclinical model.

Specifically, a tumor growth delay study demonstrated no differences in the growth of tumors treated either immediately or with a 24 hours delay between two partial irradiations.

An initial study of the effects of spatiotemporal fractionation on the histological level suggested possible differences in the response of tumors to inhomogeneous irradiation, warranting further investigation.

Appendix A

Supplemental Tables and Figures

Table A.1: **Tumor growth delay.** Parameters analyzed were the volume at the treatment start (V_0) and treatment end (day 7 post irradiation, V_7) and the area under the tumor growth curve (AUC). Values in brackets are normalized to V_0. Data are represented as mean ± SD. STF = spatiotemporal fractionation.

	Caliper-based measurement			**CT-based measurement**		
	V_0	V_7	AUC	V_0	V_7	AUC
No IR	290±18	719±61 (2.49)	3421±235 (11.81)	251±72	720±169 (2.92)	3254±724 (13.18)
Half IR	294±17	546±72 (1.86)	2876±179 (9.54)	231±47	483±138 (2.06)	2371±525 (10.14)
STF IR	285±13	244±38 (0.86)	2060±204 (7.24)	226±37	191±40 (0.85)	1568±115 (6.48)
Full IR	284±10	253±105 (0.89)	2094±343 (7.38)	245±60	203±120 (0.79)	1611± 217 (6.49)

Table A.2: **γ-H2AX quantification.** The proportion of γ-H2AX foci were analyzed at 30 minutes and 24 hours post irradiation. The first value in the "Half IR" group represents the irradiated half and the second value represents the non irradiated half. Data are represented as mean ± SD.

	γ-H2AX foci	
	30 min	24 h
No IR	3.1±0.8	
Half IR	46.1±12.9 / 2.4±0.8	10.5±3.3 / 2.9±1.2
STF IR	29.1±4.5	6.8±0.6
Full IR	40.3±7.4	9.5±1.5

Table A.3: **Microvessel density.** Microvessel density was analyzed by quantifying CD31 positive cells in the tumor microenvironment. The first value in the "Half IR" group represents the irradiated half and the second value represents the non irradiated half. Data are represented as means ± SD.

	CD31 positive cells
No IR	5.1±1.3
Half IR	9.5±3.2 / 5.1±0.9
STF IR	5.3±2.3 / 6.1±1.7
Full IR	6.9±2.7

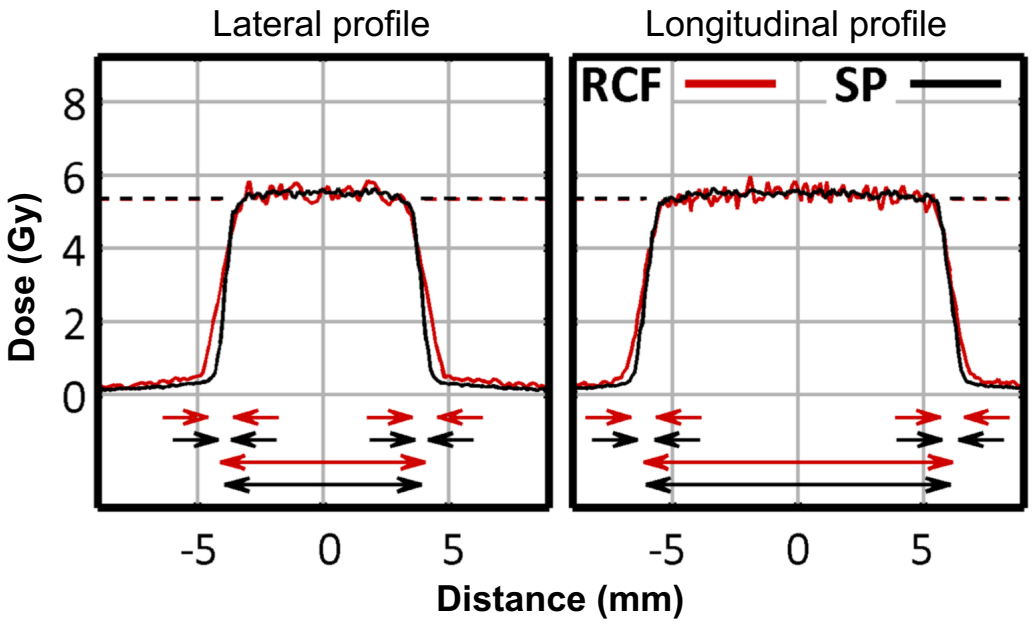

Figure A.1: **Dose profiles of the R8-12 collimator from the commissioning report.** Arrows pointing towards each other indicate the penumbra. Double headed arrows indicated beam dimensions. RCF = radiochromic film, SP = SmART-Plan.

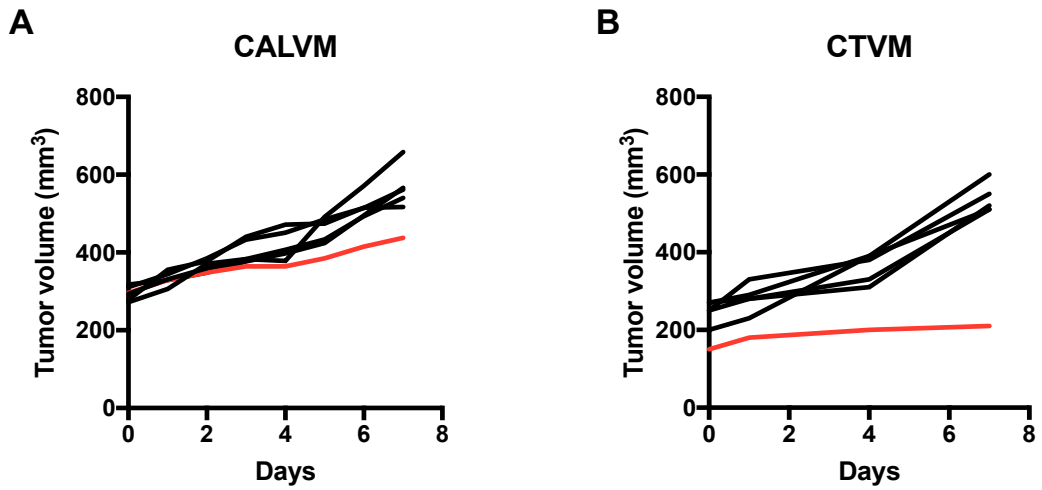

Figure A.2: **Caliper- versus CT-based tumor growth curves for partially irradiated tumors.** A: Caliper-based volumetry (CALVM) detected no outliers in the partially irradiated group (Half IR group). B: CT-based volumetry (CTVM) detected an outlier (marked red in both A and B).

Appendix B

Pipeline for Partial Tumor Irradiation

B.1 First Irradiation

1. Put the mouse under anesthesia.
2. Perform scout CT to correct the isocenter position. Perform CT scan ("Mouse Soft Tissue Mid Dose" preset).
3. Open the CT in SmART-Plan and verify the tissue segmentation ("CT2MD" tab).
4. Contour the target.
5. Add two opposing laterolateral 8 x 12 mm beams such that the target is fully covered and the normal tissue is spared.
6. Reposition the isocenter to be in the tissue and as close as possible to the center of the target.
7. Set the prescribed dose to 12 Gy and initiate dose calculation.
8. Adjust the treatment time directly in the .ini file such that the median dose to the tumor corresponds to the prescribed dose.
9. Export the resulting dose distribution ("DICOM Export" tool).
10. Insert the 8 x 12 mm collimator (mind the orientation) and the treatment filter. Initiate treatment.
11. Allow the mouse to regain consciousness and recover on a heating pad.
12. Import the CT data and the dose distribution into MIM. Set the prescribed dose to 12 Gy and convert the 25% isodose line into a contour ("Convert to Contour" tool in the "Dose" tab.).

B.2 Second Irradiation

1. Put the mouse under anesthesia.
2. Perform scout CT to correct the isocenter position. Perform CT scan ("Mouse Soft Tissue Mid Dose" preset).
3. Import the new CT into MIM and perform image alignment. Adjust manually as needed. Save the registered 25% isodose contour to the new CT.

4. Export data and transfer to SmART-Plan.
5. Open the new CT in SmART-Plan. Import the 25% isodose contour with the "Import DICOM" → "RTSTRUCT" tool.
6. Process as with the first irradiation.

Bibliography

[1] Parveen Kumar and Michael L Clark. *Kumar and Clark's Clinical Medicine*. Elsevier Health Sciences, 2012.

[2] International Agency for Research on Cancer. Globocan 2018. `http://gco.iarc.fr/today/fact-sheets-cancers`. Accessed: 2018-09.

[3] Douglas Hanahan and Robert A Weinberg. The hallmarks of cancer. *Cell*, 100(1):57–70, 2000.

[4] Douglas Hanahan and Robert A Weinberg. Hallmarks of cancer: The next generation. *Cell*, 144(5):646–674, 2011.

[5] MD Anderson Cancer Center. Cancer treatment options: Surgery. `https://www.mdanderson.org/treatment-options/surgery.html`. Accessed: 2018-09.

[6] Eric J Hall, Amato J Giaccia, et al. *Radiobiology for the Radiologist*, volume 6. Lippincott Williams & Wilkins Philadelphia, 2006.

[7] Louai Labanieh, Robbie G Majzner, and Crystal L Mackall. Programming car-t cells to kill cancer. *Nature Biomedical Engineering*, 2(6):377, 2018.

[8] Charles Sawyers. Targeted cancer therapy. *Nature*, 432(7015):294, 2004.

[9] Rajamanickam Baskar, Kuo Ann Lee, Richard Yeo, and Kheng-Wei Yeoh. Cancer and radiation therapy: current advances and future directions. *Int J Med Sci*, 9(3):193–199, 2012.

[10] Frank Herbert Attix. *Introduction to radiological physics and radiation dosimetry*. John Wiley & Sons, 2008.

[11] Michael Goitein. *Radiation oncology: a physicist's-eye view*. Springer Science & Business Media, 2007.

[12] Frank Verhaegen, Patrick Granton, and Erik Tryggestad. Small animal radiotherapy research platforms. *Physics in medicine and biology*, 56(12):R55, 2011.

[13] nuclear power.net. Interaction of gamma radiation with matter. `https://www.nuclear-power.net/nuclear-power/reactor-physics/interaction-radiation-matter/interaction-gamma-radiation-matter/`. Accessed: 2018-09.

[14] Hedi Fritz-Niggli. *Strahlengefährdung, Strahlenschutz: ein Leitfaden für die Praxis*. Huber, 1991.

[15] Michael C Joiner and Albert Van der Kogel. *Basic clinical radiobiology*, volume 1. CRC press, 2016.

[16] Kum Kum Khanna and Stephen P Jackson. Dna double-strand breaks: signaling, repair and the cancer connection. *Nature genetics*, 27(3):247, 2001.

[17] Emmy P Rogakou, Duane R Pilch, Ann H Orr, Vessela S Ivanova, and William M Bonner. Dna double-stranded breaks induce histone h2ax phosphorylation on serine 139. *Journal of biological chemistry*, 273(10):5858–5868, 1998.

[18] Tanya T Paull, Emmy P Rogakou, Vikky Yamazaki, Cordula U Kirchgessner, Martin Gellert, and William M Bonner. A critical role for histone h2ax in recruitment of repair factors to nuclear foci after dna damage. *Current Biology*, 10(15):886–895, 2000.

[19] Linda J Kuo and Li-Xi Yang. γ-h2ax-a novel biomarker for dna double-strand breaks. *In vivo*, 22(3):305–309, 2008.

[20] William M Bonner, Christophe E Redon, Jennifer S Dickey, Asako J Nakamura, Olga A Sedelnikova, Stéphanie Solier, and Yves Pommier. γh2ax and cancer. *Nature Reviews Cancer*, 8(12):957, 2008.

[21] Dietmar W Siemann. The unique characteristics of tumor vasculature and preclinical evidence for its selective disruption by tumor-vascular disrupting agents. *Cancer treatment reviews*, 37(1):63–74, 2011.

[22] Noel Weidner. Intratumor microvessel density as a prognostic factor in cancer. *The American journal of pathology*, 147(1):9, 1995.

[23] Saulius Svagzdys, Vaiva Lesauskaite, Dainius Pavalkis, Irena Nedzelskienė, Darius Pranys, and Algimantas Tamelis. Microvessel density as new prognostic marker after radiotherapy in rectal cancer. *BMC cancer*, 9(1):95, 2009.

[24] Coen IM Baeten, Karolien Castermans, Guido Lammering, Femke Hillen, Bradly G Wouters, Harry FP Hillen, Arjan W Griffioen, and Cornelius GMI Baeten. Effects of radiotherapy and chemotherapy on angiogenesis and leukocyte infiltration in rectal cancer. *International Journal of Radiation Oncology* Biology* Physics*, 66(4):1219–1227, 2006.

[25] Peter J Newman. The role of pecam-1 in vascular cell biology a. *Annals of the New York Academy of Sciences*, 714(1):165–174, 1994.

[26] William Small and Eric D Donnelly. Leibel and phillips textbook of radiation oncology. *JAMA*, 307(1):93–93, 2012.

[27] Howard D Thames. On the origin of dose fractionation regimens in radiotherapy. In *Seminars in Radiation Oncology*, volume 2, pages 3–9. Elsevier, 1992.

[28] H Rodney Withers. The four r's of radiotherapy. In *Advances in radiation biology*, volume 5, pages 241–271. Elsevier, 1975.

[29] G Gordon Steel, Trevor J McMillan, and JH Peacock. The 5rs of radiobiology. *International journal of radiation biology*, 56(6):1045–1048, 1989.

[30] Elaine M Zeman. The history and radiobiology of hypofractionation. In *Hypofractionated and Stereotactic Radiation Therapy*, pages 1–31. Springer, 2018.

[31] W Dörr. Radiobiology of tissue reactions. *Annals of the ICRP*, 44(1_suppl):58–68, 2015.

[32] Karen K Fu, Thomas F Pajak, Andy Trotti, Christopher U Jones, Sharon A Spencer, Theodore L Phillips, Adam S Garden, John A Ridge, Jay S Cooper, K Kian Ang, et al. A radiation therapy oncology group (rtog) phase iii randomized study to compare hyperfractionation and two variants of accelerated fractionation to standard fractionation radiotherapy for head and neck squamous cell carcinomas: first report of rtog 9003. *International Journal of Radiation Oncology* Biology* Physics*, 48(1):7–16, 2000.

[33] Michele Saunders, Stanley Dische, Ann Barrett, Angela Harvey, Gareth Griffiths, and Mahesh Parmar. Continuous, hyperfractionated, accelerated radiotherapy (chart) versus conventional radiotherapy in non-small cell lung cancer: mature data from the randomised multicentre trial. *Radiotherapy and oncology*, 52(2):137–148, 1999.

[34] SM Bentzen, RK Agrawal, EG Aird, JM Barrett, PJ Barrett-Lee, JM Bliss, J Brown, JA Dewar, HJ Dobbs, JS Haviland, et al. The uk standardisation of breast radiotherapy (start) trial b of radiotherapy hypofractionation for treatment of early breast cancer: a randomised trial. *Lancet (London, England)*, 371(9618):1098–1107, 2008.

[35] F Ellis. Nominal standard dose and the ret. *The British journal of radiology*, 44(518):101–108, 1971.

[36] Colin G Orton and Lionel Cohen. A unified approach to dose-effect relationships in radiotherapy. i: Modified tdf and linear quadratic equations. *International Journal of Radiation Oncologyâ¢ Biologyâ¢ Physics*, 14(3):549–556, 1988.

[37] GW Barendsen. Dose fractionation, dose rate and iso-effect relationships for normal tissue responses. *International Journal of Radiation Oncology* Biology* Physics*, 8(11):1981–1997, 1982.

[38] John F Fowler. The linear-quadratic formula and progress in fractionated radiotherapy. *The British journal of radiology*, 62(740):679–694, 1989.

[39] Jack F Fowler. 21 years of biologically effective dose. *The British journal of radiology*, 83(991):554–568, 2010.

[40] DE Lea and DG Catcheside. The mechanism of the induction by radiation of chromosome aberrations intradescantia. *Journal of genetics*, 44(2-3):216–245, 1942.

[41] Bleddyn Jones. Mathematical models of tumour and normal tissue response. *Acta oncologica*, 38(7):883–893, 1999.

[42] David J Brenner, Lynn R Hlatky, Philip J Hahnfeldt, Eric J Hall, and Rainer K Sachs. A convenient extension of the linear-quadratic model to include redistribution and reoxygenation. *International Journal of Radiation Oncologyâ¢ Biologyâ¢ Physics*, 32(2):379–390, 1995.

[43] Jian Z Wang, Zhibin Huang, Simon S Lo, William TC Yuh, and Nina A Mayr. A generalized linear-quadratic model for radiosurgery, stereotactic body radiation therapy, and high–dose rate brachytherapy. *Science translational medicine*, 2(39):39ra48–39ra48, 2010.

[44] Clint Park, Lech Papiez, Shichuan Zhang, Michael Story, and Robert D Timmerman. Universal survival curve and single fraction equivalent dose: useful tools in understanding potency of ablative radiotherapy. *International Journal of Radiation Oncology* Biology* Physics*, 70(3):847–852, 2008.

[45] B Jones, RG Dale, C Deehan, KI Hopkins, and DAL Morgan. The role of biologically effective dose (bed) in clinical oncology. *Clinical oncology*, 13(2):71–81, 2001.

[46] Jan Unkelbach, Chuan Zeng, and Martijn Engelsman. Simultaneous optimization of dose distributions and fractionation schemes in particle radiotherapy. *Medical physics*, 40(9), 2013.

[47] Jan Unkelbach and Dávid Papp. The emergence of nonuniform spatiotemporal fractionation schemes within the standard bed model. *Medical physics*, 42(5):2234–2241, 2015.

[48] Jan Unkelbach, Marc R Bussière, Paul H Chapman, Jay S Loeffler, and Helen A Shih. Spatiotemporal fractionation schemes for irradiating large cerebral arteriovenous malformations. *International Journal of Radiation Oncology* Biology* Physics*, 95(3):1067–1074, 2016.

[49] Jan Unkelbach. Non-uniform spatiotemporal fractionation schemes in photon radiotherapy. In *World Congress on Medical Physics and Biomedical Engineering, June 7-12, 2015, Toronto, Canada*, pages 401–404. Springer, 2015.

[50] Jan Unkelbach, Dávid Papp, Melissa R Gaddy, Nicolaus Andratschke, Theodore Hong, and Matthias Guckenberger. Spatiotemporal fractionation schemes for liver stereotactic body radiotherapy. *Radiotherapy and Oncology*, 125(2):357–364, 2017.

[51] Melissa R Gaddy, Sercan Yıldız, Jan Unkelbach, and Dávid Papp. Optimization of spatiotemporally fractionated radiotherapy treatments with bounds on the achievable benefit. *Physics in Medicine & Biology*, 63(1):015036, 2018.

[52] Faiz M Khan and John P Gibbons. *Khan's the physics of radiation therapy.* Lippincott Williams & Wilkins, 2014.

[53] Frank Verhaegen, James Stewart, and David Jaffray. Developing technologies for small animal radiotherapy. In *Handbook of Small Animal Imaging: Preclinical Imaging, Therapy, and Applications*, pages 329–351. CRC Press, 2016.

[54] CT Badea, M Drangova, DW Holdsworth, and GA Johnson. In vivo small-animal imaging using micro-ct and digital subtraction angiography. *Physics in medicine and biology*, 53(19):R319, 2008.

[55] Stephanie K Carlson, Kelly L Classic, Claire E Bender, and Stephen J Russell. Small animal absorbed radiation dose from serial micro-computed tomography imaging. *Molecular Imaging and Biology*, 9(2):78–82, 2007.

[56] Fred A Mettler Jr, Walter Huda, Terry T Yoshizumi, and Mahadevappa Mahesh. Effective doses in radiology and diagnostic nuclear medicine: a catalog. *Radiology*, 248(1):254–263, 2008.

[57] Frank Verhaegen. Treatment planning for small animals. In *Handbook of Small Animal Imaging: Preclinical Imaging, Therapy, and Applications*, pages 365–384. CRC Press, 2016.

[58] Stefan J van Hoof, Patrick V Granton, and Frank Verhaegen. Development and validation of a treatment planning system for small animal radiotherapy: Smart-plan. *Radiotherapy and Oncology*, 109(3):361–366, 2013.

[59] Magdalena Bazalova and Edward E Graves. The importance of tissue segmentation for dose calculations for kilovoltage radiation therapy. *Medical physics*, 38(6):3039–3049, 2011.

[60] Joseph F Weiss and Michael R Landauer. Protection against ionizing radiation by antioxidant nutrients and phytochemicals. *Toxicology*, 189(1-2):1–20, 2003.

[61] Paul Okunieff, Yuhchyau Chen, David J Maguire, and Amy K Huser. Molecular markers of radiation-related normal tissue toxicity. *Cancer and Metastasis Reviews*, 27(3):363–374, 2008.

[62] ICRU Prescribing. recording and reporting photon beam therapy (supplement to icru report 50). *ICRU report*, 62, 1999.

[63] International Commission on Radiation Units and Measurements. *ICRU report 83 prescribing, recording, and reporting photon-beam intensity-modulated radiation therapy (IMRT)-Journal of the ICRU-vol 10 no 1 2010.* Oxford University Press, 2010.

[64] Barbara Zitova and Jan Flusser. Image registration methods: a survey. *Image and vision computing*, 21(11):977–1000, 2003.

[65] He Wang, Lei Dong, Jennifer O'Daniel, Radhe Mohan, Adam S Garden, K Kian Ang, Deborah A Kuban, Mark Bonnen, Joe Y Chang, and Rex Cheung. Validation of an accelerated âdemonsâ algorithm for deformable image registration in radiation therapy. *Physics in Medicine & Biology*, 50(12):2887, 2005.

[66] David M Euhus, Charles Hudd, Marie C Laregina, and Frank E Johnson. Tumor measurement in the nude mouse. *Journal of surgical oncology*, 31(4):229–234, 1986.

[67] Mary M Tomayko and C Patrick Reynolds. Determination of subcutaneous tumor size in athymic (nude) mice. *Cancer chemotherapy and pharmacology*, 24(3):148–154, 1989.

[68] P Workman, EO Aboagye, F Balkwill, A Balmain, Gail Bruder, DJ Chaplin, JA Double, J Everitt, DAH Farningham, MJ Glennie, et al. Guidelines for the welfare and use of animals in cancer research. *British journal of cancer*, 102(11):1555–1577, 2010.

[69] Yuta Shibamoto, Akifumi Miyakawa, Shinya Otsuka, and Hiromitsu Iwata. Radiobiology of hypofractionated stereotactic radiotherapy: what are the optimal fractionation schedules? *Journal of radiation research*, 57(S1):i76–i82, 2016.

[70] Jian Z Wang, X Allen Li, Warren D D'Souza, and Robert D Stewart. Impact of prolonged fraction delivery times on tumor control: a note of caution for intensity-modulated radiation therapy (imrt). *International Journal of Radiation Oncology* Biology* Physics*, 57(2):543–552, 2003.

[71] Jack F Fowler, James S Welsh, and Steven P Howard. Loss of biological effect in prolonged fraction delivery. *International Journal of Radiation Oncology* Biology* Physics*, 59(1):242–249, 2004.

[72] Xiao-Kang Zheng, Long-Hua Chen, Wen-Jun Wang, Feng Ye, Jia-Bing Liu, Qi-Sheng Li, and Hen-Wen Sun. Impact of prolonged fraction delivery times simulating imrt on cultured nasopharyngeal carcinoma cell killing. *International Journal of Radiation Oncology* Biology* Physics*, 78(5):1541–1547, 2010.

[73] Ling Jiang, Xiao-Peng Xiong, Chao-Su Hu, Zhou-Luo Ou, Guo-Pei Zhu, and Hong-Mei Ying. In vitro and in vivo studies on radiobiological effects of prolonged fraction delivery time in a549 cells. *Journal of radiation research*, 54(2):230–234, 2012.

[74] Natalka Suchowerska, Martin A Ebert, David R McKenzie, and Michael Jackson. A review of in vitro experimental evidence for the effect of spatial and temporal modulation of radiation dose on response. *Acta oncologica*, 49(8):1344–1353, 2010.

[75] Takayoshi Ishimori, Mitsuaki Tatsumi, and Richard L Wahl. Tumor response assessment is more robust with sequential ct scanning than external caliper measurements1. *Academic radiology*, 12(6):776–781, 2005.

[76] Mette Munk Jensen, Jesper Tranekjær Jørgensen, Tina Binderup, and Andreas Kjær. Tumor volume in subcutaneous mouse xenografts measured by microct is more accurate and reproducible than determined by 18 f-fdg-micropet or external caliper. *BMC medical imaging*, 8(1):16, 2008.

[77] Larry Norton. A gompertzian model of human breast cancer growth. *Cancer research*, 48(24 Part 1):7067–7071, 1988.

[78] Anna Kane Laird. Dynamics of tumour growth. *British journal of cancer*, 18(3):490, 1964.

[79] Carmel Mothersill and CB Seymour. Cell-cell contact during gamma irradiation is not required to induce a bystander effect in normal human keratinocytes: evidence for release during irradiation of a signal controlling survival into the medium. *Radiation research*, 149(3):256–262, 1998.

[80] N Suchowerska, Martin A Ebert, M Zhang, and M Jackson. In vitro response of tumour cells to non-uniform irradiation. *Physics in Medicine & Biology*, 50(13):3041, 2005.

[81] E Claridge Mackonis, N Suchowerska, M Zhang, M Ebert, DR McKenzie, and M Jackson. Cellular response to modulated radiation fields. *Physics in Medicine & Biology*, 52(18):5469, 2007.

[82] E Claridge Mackonis, N Suchowerska, DR McKenzie, M Ebert, M Jackson, S Morrell, and J Bewes. Reply to âcomments on âcellular response to modulated radiation fieldsââ. *Physics in Medicine & Biology*, 54(5):L15, 2009.

[83] Karl T Butterworth, Conor K McGarry, Colman Trainor, Stephen J McMahon, Joe M OâSullivan, Giuseppe Schettino, Alan R Hounsell, and Kevin M Prise. Dose, dose-rate and field size effects on cell survival following exposure to non-uniform radiation fields. *Physics in Medicine & Biology*, 57(10):3197, 2012.

[84] Chung-Hyun Cho, Richard A Kammerer, Hyuek Jong Lee, Kunio Yasunaga, Kyung-Tae Kim, Han-Ho Choi, Won Kim, Sung Hyun Kim, Sung Kwang Park, Gyun Min Lee, et al. Designed angiopoietin-1 variant, comp-ang1, protects against radiation-induced endothelial cell apoptosis. *Proceedings of the National Academy of Sciences*, 101(15):5553–5558, 2004.

[85] Jeff H Tsai, Sosina Makonnen, Michael Feldman, Chandra Sehgal, Amit Maity, and William MF Lee. Ionizing radiation inhibits tumor neovascularization by inducing ineffective angiogenesis. *Cancer biology & therapy*, 4(12):1395–1400, 2005.

[86] B Chen, ZHENJUN Zhao, N Raoufi-Rad, V Lee, M Grace, R Reddy, and M Stoodley. Radiation-induced expression of platelet endothelial cell adhesion molecule-1 in cerebral endothelial cells. *International Journal of Radiation Research*, 14(3):181, 2016.

[87] G Karamanolis, I Delladetsima, V Kouloulias, K Papaxoinis, I Panayiotides, D Haldeopoulos, K Triantafyllou, N Kelekis, and SD Ladas. Increased expression of vegf and cd31 in postradiation rectal tissue: implications for radiation proctitis. *Mediators of inflammation*, 2013, 2013.

[88] Steven Quarmby, Pat Kumar, JiMin Wang, Janet A Macro, Jerry J Hutchinson, Robin D Hunter, and Shant Kumar. Irradiation induces upregulation of cd31 in human endothelial cells. *Arteriosclerosis, thrombosis, and vascular biology*, 19(3):588–597, 1999.

[89] Steven Quarmby, Robin D Hunter, and Shant Kumar. Irradiation induced expression of cd31, icam-1 and vcam-1 in human microvascular endothelial cells. *Anticancer research*, 20(5B):3375–3381, 2000.

[90] Marc P Pusztaszeri, Walter Seelentag, and Fred T Bosman. Immunohistochemical expression of endothelial markers cd31, cd34, von willebrand factor, and fli-1 in normal human tissues. *Journal of Histochemistry & Cytochemistry*, 54(4):385–395, 2006.